# Characterization of oxide scales formed on alloy 82 in nominal PWR primary water at 340 °C and in hydrogenated steam at 400 °C

Cecilie Duhamel, Mohamed Sennour, Frédéric Georgi, Catherine Guerre, Elizabeth Chaumun, Jérôme Crépin, Eva Héripré, Ian De Curières

# Characterization of oxide scales formed on Alloy 82 in nominal PWR primary water at 340°C and in hydrogenated steam at 400°C

C. Duhamel [a,*], M. Sennour [a], F. Georgi [b], C. Guerre [c], E. Chaumun [a,c], J. Crépin [a], E. Héripré [d], I. de Curières [e]

[a] *MINES ParisTech, PSL - Research University, MAT - Centre des matériaux, CNRS UMR 7633, BP 87, 91003 Evry Cedex, France*

[b] *MINES ParisTech, PSL - Research University, CEMEF - Centre de mise en forme des matériaux, CNRS UMR 7635, CS 10207 rue Claude Daunesse, 06904 Sophia-Antipolis Cedex, France*

[c] *CEA, DEN, DPC, SCCME, Laboratoire d'Etude de la Corrosion Aqueuse, F-91191 Gif-sur-Yvette, France.*

[d] *Ecole Polytechnique, Laboratoire de Mécanique des Solides, CNRS UMR 7649, 91128 Palaiseau cedex, France*

[e] *Institute for Radiological Protection and Nuclear Safety (IRSN), DSR/SAMS, BP17, 92262 Fontenay-aux-Roses Cedex, France*

## ABSTRACT

Alloy 82, used as weld metal in Pressurized Water Reactor (PWR), is exposed to hydrogenated steam at 400°C and to simulated primary water at 340°C. A comparative study of the oxide layer formed on the alloy surface in both environments is performed to confirm that steam conditions are representative of accelerated primary water conditions. For this purpose, the oxidation products are investigated at a nanometer scale using Scanning Electron Microscopy (SEM), X-ray Photoelectron Spectrometry (XPS) and Transmission Electron Microscopy (TEM). Results obtained in both conditions are compared and the influences of heat treatment, test duration and surface preparation are studied.

[*] Corresponding author
Tel: (+33) 1 60 76 30 65
e-mail: cecilie.duhamel@mines-paristech.fr

## 1. Introduction

Nickel base austenitic alloys are widely used in nuclear primary water reactors (PWR) either as wrought materials or as weldments. Although Alloy 600 (Ni-15Cr-10Fe) is known since the late 1950s [1] to be susceptible to primary water stress corrosion cracking (PWSCC), the first crack initiations in its weld material Alloy 182 were detected in 1994 [2]. To date, more than 300 cases have been reported mostly in Alloy 182 (13-17 wt.% Cr) but few events of cracking are also documented for Alloy 82 (18-22 wt.%Cr) [3-5]. In addition, only welds that are not stress-relieved by the thermal treatment applied to the adjacent low carbon steel components are affected and cracking occurs in regions with high residual stresses [2,6].

During laboratory tests, initiation of stress corrosion cracks in Alloy 82 in simulated primary water may require long exposure times of several thousands of hours, even at 360°C [7]. Economy et al. [8] showed that a tenfold decrease in PWSCC initiation time is obtained in Alloy 600 by performing SCC tests in hydrogenated steam at 400°C instead of primary water at 360°C. Their results suggest that no significant modification of the SCC mechanisms occur when going through the phase boundary from water to steam as: (i) the SCC cracks exhibit similar features in both environments, (ii) comparison between several heats gives similar trends and (iii) the SCC initiation time follows the same Arrhenius relationship over a temperature range covering both the liquid and vapor phases.

SCC propagation and initiation tests performed on several Alloy 82 welds in hydrogenated steam at 400°C show that the SCC susceptibility depends on the chemical composition of the weld and/or the welding process [9]. In addition, a heat treatment simulating the in-service stress-relief treatment increases the SCC resistance [9,10]. The beneficial effect of the thermal treatment may result from intergranular chromium carbide precipitation [11,12], which is already known to improve the SCC resistance in Alloy 600 [13].

The properties of the oxide scale that forms at the surface of the nickel base alloys in primary water are also likely to play a key role in the SCC mechanism [14]. Although detailed descriptions of the oxide layers formed at the surface of Alloys 600 and 690 in primary water have been extensively reported in the literature [15-20], fewer data exist for nickel base welds [21,22] most probably because their oxidation behavior is assumed to be similar to that of the wrought alloys. Oxidation of Alloy 600 in PWR conditions leads to the formation of a duplex oxide layer with a discontinuous outer layer covering a continuous Cr-rich inner layer. The outer layer consists of nickel ferrite ($NiFe_2O_4$) crystallites coming mainly from the saturation of the water in Fe and Ni cations. The presence of nickel hydroxide $Ni(OH)_2$ is sometimes

reported [15,17,23]. The inner layer is constituted of mixed nickel and iron chromite $Ni(Fe,Cr)_2O_4$. Some authors also report the existence of $Cr_2O_3$ either as a thin continuous layer [18] or as discontinuous nodules [15] at the oxide / alloy interface. Besides, Cr depletion of the alloy may be observed below the alloy / oxide interface [24,25].

The aims of this work are to estimate the representativeness of the hydrogenated steam environment to simulate oxidation in primary water conditions and to provide a detailed description of the oxide scales formed on Alloy 82 welds. For this purpose, oxidation tests are carried out in hydrogenated steam at 400°C and in simulated primary water at 340°C. The oxide layers are characterized using X-ray Photoelectron Spectroscopy (XPS) and analytical Transmission Electron Microscopy (TEM). The effects of post-welding thermal treatment and surface finish on the oxide layer are also studied.

## 2. Materials and experimental procedures

### *2.1. Materials and specimens*

Butt welds of Alloy 82, manufactured by Fouré-Lagadec using Gas Tungsten Arc Welding (GTAW), are deposited between two plates of 304L stainless steel. The chemical composition of Alloy 82 after welding is given in Table 1. One butt weld is studied in the as-welded conditions while the other one undergoes a heat treatment of 7h at 600°C. This heat treatment simulates the stress relief treatment applied in service to the components next to the weld. More details on the welding process conditions, weld's geometry and microstructure are given in [10,11]. In particular, it was shown that the heat treatment favors chromium carbide precipitation at the grain boundaries.

Coupons with dimensions of 50 x 9 x1.5 $mm^3$ are cut by electro-discharge machining with the weld in the middle of the sample. In order to study the influence of surface preparation on oxidation, the samples are polished to mirror finish either with 1µm diamond paste or with colloidal silica suspension.

### *2.2. Corrosion test procedure*

The corrosion experiments in pure hydrogenated steam are performed in a 23L stainless steel autoclave at 400°C and under a pressure of 200 bar with a partial pressure of hydrogen of 800 mbar. The hydrogen content is controlled by a silver-palladium probe. The corrosion experiments in simulated primary water are carried out in a 380 mL stainless steel autoclave at 340°C and with a total pressure of 144 bars. The solution contains 2 ppm lithium (as LiOH) and 1000 ppm boron (as $H_3BO_3$) and is in equilibrium with a hydrogen partial pressure of 200

mbar (dissolved hydrogen content = 37 cc / kg $H_2O$). The exposure times for both tests are 1500h and 2500h. The effects of the metallurgical state (as-welded/heat treated), environment, test duration (1500h/2500h) and surface state (1µm/OPS) are then studied.

*2.3. Experimental characterizations*

*a) SEM and TEM observations*

Scanning Electron Microscopy (SEM) observations of oxidized surfaces are performed using a field emission gun (FEG) Zeiss Ultra 55 microscope. Observations are realized in backscattered-electron mode to better distinguish the oxide from the material.

TEM observations are performed on cross-section samples. The latter are prepared by ion milling or Focused Ion Beam (FIB) techniques. More details on the ion milling preparation are given elsewhere [15]. FIB preparation is carried out by SERMA Technologies (Grenoble, France) on a dual beam FEI Strata DB400 apparatus equipped with an omniprobe. Sample surfaces are first protected by a tungsten coating. FIB preparation allows observing large (20 x 10 µm) and thin (~ 100 nm) areas. However, ion milling preparation allows observing smaller areas but with very thin zone (< 50 nm) at the extreme surface, which is more suitable for High-Resolution TEM (HRTEM) observations.

TEM investigations are realized on a FEI TECNAI F20-ST field emission gun microscope equipped with an Energy Dispersive X-ray (EDX) device, a Scanning TEM (STEM) system and High-Angle Annular Dark Field (HAADF) detector. STEM-HAADF combination allows obtaining chemical contrast (Z-contrast) images with a high spatial resolution. Elemental EDX analysis is performed in both positional and line-scan modes using a nanometer-sized probe (1-2 nm). Crystallographic structure of oxides is investigated using HRTEM imaging. Local area fast Fourier transform (FFT) diffractograms are calculated on HRTEM images and indexed as electron diffraction patterns. Electron diffraction is also carried out when possible, especially on large particles. A systematic combination of lattice imaging (HRTEM) and chemical analysis (EDX) is applied in order to clearly identify oxides structure and composition.

*b) XPS analysis*

X-ray Photoelectron Spectroscopy (XPS) analyses are carried out using a Thermo-Fischer K-alpha spectrometer with a monochromatic Al Kα source. The analyses are performed on all

the samples with a 1 µm finish oxidized in hydrogenated steam. No XPS characterization of the oxide layers formed in primary water are carried out.

Depth profiles are obtained by sputtering the surface with a monoatomic $Ar^+$ ion beam. An ellipsoid surface of 300×600 µm² is analyzed in the center of the 1×2 mm² sputtered surface. The crater depth is measured using a Dektak 8 stylus profilometer. The mean sputtering rate, measured on 8 different craters, is estimated to 0.6 $nm.s^{-1}$. The sputtering rates of the oxide and the alloy are assumed to be similar. During XPS analysis, a low energy flood-gun is used in order to reduce the charge effect that can be present on the less conductive oxide layer on surface. The pass energy is 40 eV for the detailed spectra.

## 3. Results

### *3.1. Oxidation in hydrogenated steam*

#### *3.1.1. SEM observations*

SEM investigations of the surfaces of coupons exposed to hydrogenated steam show that the oxide layer is composed of a continuous layer on which a variety of crystallites are dispersed (Fig. 1). The latter are of different shapes and sizes but may be divided into two families: (i) large pyramidal particles which can reach one micrometer in size and (ii) platelet-like particles with relatively smaller sizes.

The comparison between the different samples shows that the density of crystallites varies from one sample to another whereas the continuous compact layer seems to be similar on all of them. Considering the as-welded sample exposed 2500h (Fig. 1a) as a reference, it can be noticed that the heat treatment reduces the platelet-like particles density whereas it increases the density of the pyramidal ones (Fig. 1b). For a shorter exposition time, we notice an increase of both platelet-shaped and pyramidal crystallites density (Fig. 1c). At last, an increase of the number and the size of the pyramidal crystallites is observed after colloidal silica suspension finish (Fig. 1d) compared to a 1 µm diamond paste finish. The effect of the final polishing on the platelet-shaped crystallites is less obvious.

#### *3.1.2. XPS analyses*

XPS analyses are performed on all the samples with a 1 µm finish oxidized in hydrogenated steam. The following XPS spectra are recorded for sputtering times ranging between 0 and 200s: C 1s, O 1s, Cr 2p, Fe 2p, Mn 2p, Mn 3p, Ni 2p and Nb 3d.

In the following, the XPS spectra are gathered in 2D stacked charts for a given element. An intensity offset is applied and relative intensities are used to better distinguish the energy evolution with sputtering time. Only the results obtained on the as-welded sample exposed 2500h will be described in detail as similar results are obtained for the two other samples.

*Ni 2p spectra:*

The Ni 2p spectra are shown in Fig. 2a. Before sputtering (t=0s), the Ni 2p spectrum consists of the $2p_{3/2}$ peak (peak 2) and its shake-up satellite (peak $*_2$) at binding energies of 855.8 eV and 861.6 eV, respectively. Additional peaks at binding energies of 873.0 eV (peak 1) and 879.4 eV (peak $*_1$) corresponding to the $2p_{1/2}$ peak and its shake-up satellite are also observed. These binding energies are consistent with the oxidation state +II of nickel [26]. The nickel-containing oxides that may be encountered at the surface of Alloy 82 oxidized in the conditions used here are NiO, $Ni(OH)_2$ and/or $NiFe_{2-x}Cr_xO_4$ ($0 \leq x \leq 2$). A selection of binding energies reported in the literature for Ni $2p_{3/2}$ spectra obtained on these nickel oxides and hydroxides is given in Table 2. The Ni 2p spectrum before sputtering is compared to the Ni 2p spectrum recorded in similar conditions on nickel oxide NiO obtained by high temperature oxidation of pure nickel. The decomposition of the $Ni^{2+}$ $2p_{3/2}$ peak in NiO gives a main peak at 854.0 eV, a second peak at 855.8 eV and a satellite peak at 861.2 eV which is in perfect agreement with data from the literature [27,28]. As for NiO, the shape of the $2p_{3/2}$ peak obtained on oxidized Alloy 82 before sputtering is large, asymmetric with a significant component in the high energy side. However, the binding energy is slightly higher than for NiO. The shape and the binding energies of the $2p_{3/2}$ peak are consistent with that of $NiFe_2O_4$. As shown by [29,30], the Ni 2p spectrum for $NiFe_2O_4$ consists of two main peaks that partially superimpose in the energy range [854.7 eV; 856.8 eV] leading to a shouldering in the high energy side. Similar superimposition of several peaks is observed for $NiCr_2O_4$ but, in this case, the shouldering occurs in the low energy side.

Signal coming from the contribution of $Ni(OH)_2$, which gives a symmetric peak at a binding energy of 856.2-856.8 eV [17,29-32], may also contribute to the $2p_{3/2}$ peak obtained before sputtering.

For sputtering times of 10s and 30s, the intensities of the peaks corresponding to the oxidation state of nickel strongly decrease while two additional peaks, characteristic of metallic nickel

[26,28,33], appear at binding energies of 852.6 eV (peak 2') and 869.9 eV (peak 1'). For longer sputtering times ($t \geq 50s$), the peaks coming from $Ni^{2+}$ completely disappear. Only the signal for metallic nickel remains. The shake-up satellite peaks of $Ni^0$ $2p_{3/2}$ and $Ni^0$ $2p_{1/2}$ are observed at binding energies of 858.6eV (peak $*_{2'}$) and 874.3 eV (peak $*_{1'}$) which is again consistent with literature [26,28,33]. The strong and sudden decrease of the $Ni^{2+}$ signal with sputtering is also observed by Liu et al. [21] for Alloy 182 oxidized at 300°C in primary water for one week. The authors suggest that nickel is not corroded during exposure to primary water and attribute the $Ni^{2+}$ signal detected before sputtering to the formation of a very thin layer of $Ni(OH)_2$ by reaction of nickel with water vapor in air. However, as mentioned previously, the presence of nickel containing oxides, either in the form of NiO, $Ni(OH)_2$ or mixed spinel with iron and chromium, is reported for nickel base alloys [18]. Another explanation may be the reduction of oxidized nickel to metallic nickel due to ion bombardment. This chemical reduction was observed during NiO sputtering while no reduction of $Ni(OH)_2$ to Ni was reported [32]. The authors found no data on the possible reduction of spinel oxide to Ni.

*Fe 2p spectra:*

The analysis of Fe 2p spectra is more difficult than that of the other transition metals as: (i) strong nickel Auger peaks are likely to overlap the Fe $2p_{3/2}$ peak and (ii) two oxidation states exist: ferrous (oxidation state + II) and ferric (oxidation state +III). Besides, some oxides such as $Fe_3O_4$ have mixed oxidation states. The two oxidation states differ by their binding energies, peak shape and shake-up satellite position. In addition, for a given oxidation state, the chemical environment also affects these features. The binding energies of $Fe^{3+}(2p_{3/2})$ in $Fe_2O_3$ and of $Fe^{2+}(2p_{3/2})$ in FeO are 711.0 eV and 709.5 eV, respectively [36]. The satellite peak of $Fe^{3+}(2p_{3/2})$ is located at nearly 8 eV higher energy than the $Fe^{3+}(2p_{3/2})$ whereas the separation between the $Fe^{2+}(2p_{3/2})$ peak and its satellite is approximately 6 eV [34,36]. For $Fe_3O_4$ where the two oxidation states of iron exist, the binding energy of $Fe(2p_{3/2})$ is in the range 708.3 - 710.6 eV and no satellite is observed [36,37]. For a given oxidation state, the chemical environment also affects binding energies, peak shape and shake-up satellite intensity. Indeed, a slight shift of the $Fe^{3+}(2p_{3/2})$ peak towards lower binding energies (0.2-0.4 eV) is observed for $NiFe_xCr_{2-x}O_4$ spinel oxides compared to $Fe_2O_3$ while no satellite peak is detected [29,34,36]. The binding energies of $Fe_xCr_{3-x}O_4$ (with $1 \leq x < 3$) range between that of $Fe^{3+}(2p_{3/2})$ in $Fe_2O_3$ and of $Fe^{2+}(2p_{3/2})$ in FeO and no satellite peak is observed except for $FeCr_2O_4$ [34].

A series of Fe 2p spectra obtained on our sample is shown in Fig. 2b. Before sputtering, the Fe 2p spectrum consists of two peaks with binding energies of 711.2 eV ($2p_{3/2}$ – peak 4) and 723.9 eV ($2p_{1/2}$ – peak 3). No shake-up satellites are detected. The binding energies as well as the absence of satellite peaks are consistent with the presence of spinel oxides such as $NiFe_xCr_{2-x}O_4$ or $Fe_xCr_{3-x}O_4$. After 10s and 30s of sputtering, a slight shift (~ -1 eV) of both the $2p_{3/2}$ and $2p_{1/2}$ peaks towards the lower energies is observed. Besides, a shake-up satellite (peak $*_3$) located at approximately 8 eV higher energy than the $2p_{1/2}$ peak appears and a shouldering around 715 eV is observed on the high energy side of the $2p_{3/2}$ peak. The energy shift could be attributed to a decrease of iron-to-chromium ratio in the spinel [34]. However, this would not explain the existence of the shake-up satellites, except if $FeCr_2O_4$ is formed. Another possibility is that the ferrous ions of the spinel are being reduced into ferric ions during ion bombardment. The formation of FeO would thus explain both the energy shift and the presence of the shake-up satellites [36]. For longer sputtering times ($t \geq 50s$), detailed analysis of the Fe 2p spectra becomes difficult as the strong Auger peaks from nickel dominate at 706 eV and 712 eV (peaks $A_{Ni}$ and $A'_{Ni}$) [26] and superimpose to the $Fe^0(2p_{3/2})$ peak. The $2p_{1/2}$ peak of iron in an oxidized state is no more detected while the $Fe^0(2p_{1/2})$ peak (peak 3') is detected at a binding energy of 719.7 eV, although with a low intensity [26].

*Cr 2p spectra:*

The Cr 2p spectra are presented in Fig. 2c. In the outermost surface of the sample (t = 0s and 10s), chromium is mostly in an oxidized state $Cr^{3+}$ as shown by the binding energies of the $2p_{3/2}$ (576.9 eV) and $2p_{1/2}$ (588.2 eV) peaks (peaks 5 and 6, respectively). These values are very close to the values reported in the literature for $Cr^{3+}$ in $Cr_2O_3$ and in iron and/or nickel chromite [17,30,34]. This makes it difficult to assess for one or the other type of oxide solely on the binding energies. Marchetti et al. [30] showed that the Cr $2p_{3/2}$ peak in $Cr_2O_3$ and $NiCr_2O_4$ can be fitted by triplet structure and that the only fitting parameter that can allow discriminating the two species is the intensity ratio $I_{peak1}/I_{peak2}$. From a sputtering time of 30s, peaks characteristic of chromium in the metallic state appear for binding energies of 574.7 eV ($Cr^0$ $2p_{3/2}$ – peak 5') and 584.5 eV ($Cr^0$ $2p_{1/2}$ – peak 4') [26]. However, even for the longest sputtering times, the signal from oxidized chromium is still detected.

*Mn 3p and Nb 3d spectra:*

Manganese and niobium, which are minor elements in Alloy 82, are also followed by XPS. For Mn, the Mn 2p and Mn 3p spectra are recorded. Only the Mn 3p spectra are shown in Fig.

3a as interactions between the Mn $2p_{3/2}$ peak (binding energies 638 – 642 eV) and Ni Auger line LM2 at 641 eV exist. Before sputtering, the Mn 3p peak (peak 8) is observed at a binding energy of 48.0 eV. After sputtering ($10 \leq t \leq 75$s), the peak is slightly shifted (-0.4 eV) towards the higher energy side probably due to a charge effect. The binding energy is consistent with the values reported by Allen et al. [34] for spinel-type oxides containing iron and/or chromium. For longer sputtering times ($t \geq 100$s), the Mn signal is hardly visible and the evolution of the binding energy cannot be followed anymore. In the scanned energy range, the Cr 3p and Fe 3p peaks are also partially detected. Their evolution with sputtering time is consistent with the observations previously made on the 2p spectra. For Fe, a shift of the 3p peak (peak 7) towards the lower energies is observed between 0s and 10s to 50s of sputtering. The binding energy of the $Cr^{3+}$ 3p peak (peak 9) remains constant but its intensity decreases with sputtering time and the $Cr^0$ 3p peak (peak 9') appears after a sputtering time of 50s.

The Nb 3d spectra are shown in Fig. 3b. For sputtering time between 0 and 30s, the $3d_{5/2}$ and $3d_{3/2}$ peaks are detected with binding energies of 207.3 eV (peak 11) and 210.0 eV (peak 10), respectively. These values are consistent with $Nb^{5+}$ oxidation state of $Nb_2O_5$ [38-40]. From a sputtering time of 50s, a second doublet appears with a 2.6 eV split. The binding energy of the $3d_{5/2}$ peak is equal to 203.3 eV (peak 11') which is consistent with the bonding energies reported for Nb bound to carbon: 203.7-203.8 eV [38,39]. Whatever the sputtering time, metallic niobium is not detected (binding energy for $Nb^0$ $3d_{5/2}$ = 202.4 eV [26,39]). This result is in agreement with previous TEM characterizations of Alloy 82 which showed strong NbC precipitation [11].

*XPS depth profiling*

The depth profiles obtained for the as-welded sample exposed 2500h to hydrogenated steam are shown in Fig. 4a as a function of sputtering time and depth. The composition is calculated using the Ni $2p_{3/2}$, Fe $2p_{1/2}$, Cr $2p_{3/2}$, Mn $2p_{1/2}$, Nb $3d_{5/3}$ and O 1s peaks. No distinction with regards to the oxidation state is made for the metallic elements. The depth is calculated assuming a constant sputtering rate of 0.6 $nm.s^{-1}$ estimated from measurements of the crater final depth using a profiler. The composition of the surface before sputtering is not shown as it mainly consists of carbon and oxygen coming from contamination.

Oxygen is detected throughout the analyzed depth. The oxygen content strongly decreases between 20 and 45 nm and then stabilizes around 20 at.%. For most of the metallic elements, a significant change in the profile shape is also observed between 20 and 45 nm and the composition stabilizes for depths higher than 45 nm. As shown by the SEM images of the

oxidized surface, the oxide scale consists of a discontinuous outer layer of large crystallites and platelet-like oxides covering a continuous inner layer. Due to surface roughness, the oxide / alloy interface is reached after different sputtering times depending on the zones leading to a smooth rather than a sharp transition from oxide to alloy on the profiles. This transition occurs between 20 and 45 nm in the profiles. In addition, for depths higher than 45 nm, the ratios of the metallic elements are consistent with the nominal composition of the alloy.

The surface roughness also leads to semi-quantitative rather than quantitative depth profiles. However, the trends observed in Fig. 4a give indication on the oxide layer composition. The oxide layer contains mainly Cr with slight amounts of Fe and Ni. Mn and Nb in the oxidized form are also detected. The chromium content in the oxide scale increases from the surface towards the oxide / alloy interface while the iron and nickel contents follow the opposite trend. The ratio O/Cr at a depth of 20 nm is consistent with $Cr_2O_3$. The evolution of the Cr and Nb contents with depth for their two oxidation states (+III and 0 for Cr, +V and +II for Nb) is shown in Fig. 4b. The O profile is added. The trends observed for the $Cr^{3+}$ and $Nb^{5+}$ profiles confirm that the oxide / alloy interface is located at a depth close to 30 – 45 nm. The signal of Cr in the oxidized state follows the O profile and both elements are detected even for the longest sputtering time. As mentioned here before, this may result from surface roughness. This may also come from internal oxidation with formation of nodules of Cr-rich oxides below the oxide / alloy interface. The evolution of the $Nb^{2+}$ signal is consistent with previous microstructural characterizations performed on that material [11] where both intragranular and intergranular niobium carbides were observed.

Based on the depth profiles and on the spectra reported previously, the oxide scale can be described as an outer layer with a spinel-type structure such as $(Ni,Fe)(Fe,Cr)_2O_4$ and an inner layer strongly enriched in chromium, possibly $Cr_2O_3$. Internal chromium oxide is also likely to exist.

*3.1.3. TEM observations*

TEM observations carried out on cross-sections prepared from coupons exposed to hydrogenated steam at 400°C are illustrated in Fig. 5. As shown by SEM observations, bright-field TEM images confirm for all the samples the duplex structure of the oxide layer composed of a continuous internal layer and a discontinuous external layer. The latter consists of large and facetted (pyramidal and cubic) crystallites with size that can reach 1 µm and smaller platelet-like crystallites with sizes of several tens of nm. The internal layer is compact

with a thickness ranging between 15 and 20 nm. The comparison between the four different samples does not reveal noticeable differences excepting maybe the higher density of large crystallites on the colloidal silica suspension finished sample (Fig. 5d). This again confirms the SEM surface observations.

Another common feature of all samples is the ultra-fine grained microstructure just beneath the oxide scale within a depth of 300 to 400 nm. Grain sizes are ranging from few tens to few hundreds of nanometers. Below, the alloy retrieves a regular microstructure with micrometric grains.

Similarly to XPS analyses and conventional TEM observations, chemical (EDX) and crystallographic (HRTEM) investigations do not reveal noticeable differences between the four samples exposed to hydrogenated steam. Thus, although the results presented below were obtained on the as-welded sample oxidized 2500h in hydrogenated steam at 400°C, they can be considered as representative of the four studied samples.

STEM-HAADF observations are coupled to nanoscale probe EDX analysis in order to identify the chemical nature of the oxidation products. The chemical contrast (Z-contrast) allowed by HAADF imaging highlights the interfacial limit between the oxide scale (dark contrast) and the matrix (bright contrast) (Fig. 6a). Few oxide penetrations are visible and second-phase particles identified as MnS (or occasionally CuS) with sizes of few tens of nm are observed in the substrate just under the oxide layer.

Using a nanometer-sized probe (1-2 nm), EDX line-scan analysis is performed across the oxide scale and the underlying alloy. The corresponding atomic concentration profiles are given in Fig. 6b.

Starting from the outermost surface to the bulk, element concentration profiles reveal that the external oxide crystallites are mainly enriched in Fe and Ni. It is worth noting that concentrations measured by EDX analysis, and especially that of oxygen, should be regarded as qualitative since only approximate corrections are applied for O–Cr interference and oxygen X-ray absorption. As regards the continuous internal oxide layer, profiles show that it is highly enriched in Cr (~ 28 at. %) with the presence of a small concentration (~ 5 at. %) of manganese. The continuous layer is also almost depleted from the other transition metallic elements. A slight Nb enrichment at the oxide /matrix interface is detected.

Underneath the oxide layer, the compositional profiles across the alloy exhibit a wavy shape with areas of nominal alloy composition separated by Cr-depleted zones. The Cr profile behavior is to be related to the local microstructure of the alloy composed of ultrafine grains, and indicates that some of them are partially Cr-depleted.

EDX analyses must be coupled to crystallographic characterizations (HRTEM and electron diffraction) for the accurate determination of the formed oxides nature. The crystallographic structure of the formed oxides is investigated using HRTEM imaging via the exploitation of the corresponding FFT diffractograms, which are equivalent to electron diffraction patterns. Fig. 7a shows an HRTEM image obtained on a large external crystallite along [110] zone axis. The corresponding FFT diffractogram (inset image) is indexed in agreement with spinel $NiFe_2O_4$-structure with lattice parameter a = 8.32 Å. In the same manner, platelet-like crystallites are equally identified as spinel $NiFe_2O_4$-structure oxides (Fig. 7b). However, the presence of Cr in these crystallites, detected by EDX analysis, suggests that it is rather mixed spinel $Ni(Fe,Cr)_2O_4$ oxides. Concerning the continuous layer, the analysis of FFT difractograms obtained on different area through the layer, reveals a duplex crystallographic structure with the inner sub-layer (10-15 nm) identified as chromia $Cr_2O_3$-structure oxide (Fig. 7c) and the outer sub-layer (~ 5-10 nm) identified as chromite $NiCr_2O_4$-structure oxide (Fig. 7b). It may be noted also that no orientation relationships between the continuous layer and the matrix, neither between the continuous and the discontinuous layers, are established.

### *3.2. Oxidation in simulated primary water*

#### *3.2.1. SEM observations*

SEM observations performed on the as-welded sample exposed 2500 h in primary water conditions (Fig. 8a) show an oxide layer globally similar to that observed on hydrogenated steam exposed sample. In fact, the oxide layer is composed of a continuous compact layer underlying a discontinuous layer. However, some differences can be noted especially concerning the outer layer. Indeed, the density of crystallites seems to be higher and the latter are mainly of pyramidal or arbitrary shape with sizes not exceeding 1 µm. The platelet-like particles are no longer present while filaments oxides have appeared. The density of crystallites seems to be similar on all the samples unlike filaments whose density depends on the specimen and is not homogeneous for the same specimen**.** In fact, the heat treated sample presents a lower amount of oxide filaments (Fig. 8b) compared to the as-welded sample. The filaments density is still lower in the heat-treated sample with a lower duration exposure of 1500 h (Fig. 8c). On the contrary, the colloidal silica suspension final polishing seems to increase the filaments density (Fig. 8d).

#### *3.2.2. TEM observations*

Two samples (as-welded and heat treated) exposed 1500h in simulated primary water were investigated. For both samples, a duplex oxide scale composed of: (i) a compact and continuous inner layer with a thickness around 20 nm and (ii) an external layer composed of filaments and crystallites are observed (Fig. 9a and 9b). Higher magnification TEM observations (Fig. 9c) highlight that the continuous layer is in turn composed of two sublayers with approximately equivalent thicknesses (~10 nm): an inner compact sublayer and an outer fine-grained sublayer. The external crystallites present facetted shapes with sizes varying from few tens of nanometers for the majority of them to few hundreds of nanometers for the larger ones. One can also note differences in the alloy microstructure under the oxide scale between the as-welded and heat treated samples. The as-welded sample presents large grains with high density of dislocations near the surface compared to the bulk while the microstructure of the heat treated sample is rather composed of ultrafine grains. These differences suggest that the initial surface states were different.

Figures 10a and 10b show STEM-HAADF images acquired on the as-welded sample. In addition to the surface layers described here before, one can interestingly note the presence of a penetrative oxidation in the form of very fine entangled filaments originating from the continuous oxide layer and forming a band of 50-60 nm of width under this layer. EDX elemental maps acquired on the framed region on Figure 10b show that the penetrative oxide filaments are chromium and oxygen-rich in agreement with a chromium oxide (Fig. 10c and d). On the other hand, elemental maps display as expected that the continuous layer contains chromium and nickel (Fig. 10e) while the external crystallites are composed of iron and nickel (Fig. 10f).

STEM-HAADF observations carried out on the heat-treated sample are presented in Figures 11a and 11b. The duplex structure of the continuous layer is highlighted and occasional sharp oxide penetrations in the substrate are clearly distinguished (Fig 11b). However, fewer penetrative oxide filaments are observed under the continuous layer compared to the as-welded sample.

In order to identify the chemical nature of the different oxides, EDX line-scan analyses are performed across the oxide layer along the solid and the dashed arrows illustrated in Fig. 11a. The corresponding compositional profiles are presented in Figs. 11c and 11d. Thus, the larger crystallites exhibiting a brighter contrast on HAADF images are identified as nickel oxides whereas the smaller crystallites are both Fe- and Ni-rich oxides. It should also be noted that EDX spectra performed on the external layer filaments revealed that they are equally enriched in nickel and oxygen in agreement with nickel oxides or nickel hydroxides.

Concerning the continuous layer, elemental concentration profiles show that the inner compact sublayer contains Cr and Ni while the outer fine-grained sublayer contains also Fe. However, neither Mn enrichment of the continuous layer nor Cr-depleted zone under the oxide scale is observed. Nb enrichment at the oxide/matrix interface has also disappeared. As regards the oxide penetrations and the penetrative oxidation, nanoprobe EDX analyses reveal that they are Cr- and O-rich in agreement with chromium oxides.

The crystallographic structures of the formed oxides are investigated using electron diffraction and HRTEM imaging. The electron diffraction pattern obtained on a large nickel oxide crystallite (Fig. 12a) is indexed in agreement with the NiO structure. However, the small external crystallites are identified as spinel $NiFe_2O_4$-structure oxides (Fig. 12b). Concerning the filaments, HRTEM images highlight their laminated structure (Fig. 12c). The analysis of the corresponding FFT diffractogram shows that the layered planes are 2.45 Å spaced, which is close to the atomic distance of {111} planes in NiO and {101} planes in both $NiO_2$ and NiOOH. The fact that it is not possible to detect hydrogen by EDX analysis does not allow determining if it is about nickel oxide or nickel hydroxide. As regards the continuous layer, it is identified as $NiCr_2O_4$–structure oxide without distinction between the inner and the outer sub-layers (Fig. 12d). HRTEM images also reveal that the penetrative oxidation is composed of oxide nano-crystals. However, it is not possible to clearly identify their crystallographic structure, and consequently, their exact chemical nature.

## 4. Discussion

### *4.1. Comparison between XPS and TEM characterizations*

Both XPS and TEM analyses were performed on the samples oxidized in hydrogenated steam. XPS is a surface characterization technique that allows analyzing large areas (several hundreds of $\mu m^2$) with a high in-depth resolution (a few nm). It is thus well-suited for oxide layer characterization. In addition, because it is a spectroscopic technique, it gives information on both the chemical composition and the chemical environment of the elements. However, accurate in-depth analyses require small-scale surface roughness. On the contrary, analytical TEM leads to very local characterizations with a resolution in the nanometer range. Both the chemical composition and the crystallographic structure can be investigated by coupling EDX and HRTEM or electron diffraction analyses. However, if the material is heterogeneous, the risk is to characterize an area which is not fully representative of the material.

XPS analyses lead to the description of a duplex oxide scale with an outer layer consisting of a spinel-type oxide containing Ni, Fe and Cr and a Cr-rich oxide, most probably $Cr_2O_3$ as an inner layer. In addition, $Cr_2O_3$ oxide penetrations are likely, as suggested by the non-negligible $Cr^{3+}$ signal detected throughout the crater depth. Based on the TEM characterizations, a schematic of the oxide layer structure formed at the surface of samples exposed at 400°C to hydrogenated steam is proposed in (Fig. 13a). The outer layer is discontinuous and consists of crystallites with a spinel-type structure, either $NiFe_2O_4$ or $NiFe_xCr_{2-x}O_4$. The inner layer is continuous with a duplex structure consisting of $NiCr_2O_4$ in the outer part and $Cr_2O_3$ in the inner part. The oxide / alloy interface is quite rough with oxide penetrations with a depth of a few tens of nm. These observations are in good agreement with the XPS analyses even though the latter do not allow resolving the triplex structure of the oxide scale. Nevertheless, the oxide structure, the composition profiles, although semi-quantitative for both techniques, as well as the oxide thickness are consistent. Small amounts of Mn and Nb are detected in both cases, and the existence of $Cr_2O_3$ penetrations, foreseen with XPS analyses, is confirmed by TEM characterizations.

*4.2. Comparison between oxidation in hydrogenated steam and in simulated primary water*

The oxide scales formed after 2500h exposure in hydrogenated steam at 400°C and after 1500h exposure in simulated primary water at 340°C are summarized in Figure 13.

The oxide scale formed in hydrogenated steam is identical after 1500h and 2500h of exposure. No evolution with time of the oxide layer duplex morphology, nature and chemical composition is observed. The thickness of the inner layer (15 to 20 nm) does not evolve either and is similar to that measured after exposure in primary water. The measured thicknesses are in agreement with the asymptotic-type kinetics measured on Alloys 600 and 690 in primary water [24,41] and with the thickness measured on mirror-polished samples of Alloy 600 exposed to primary water at 325°C [41,42]. The results suggest that exposure in hydrogenated steam, even though performed at a slightly higher temperature, does not modify significantly the oxidation kinetics. A different trend is observed by Cissé et al. [43] on a 304L austenitic stainless steel oxidized in hydrogenated steam at 400°C and in primary water at 340°C. The authors report a two to threefold increase of the oxide thickness on the steam-exposed sample and conclude on an accelerating effect of the media rather than thermal activation.

The oxide film formed in both environments consists in a discontinuous outer layer of crystallites and a 15 to 20 nm thick continuous inner layer. In hydrogenated steam, the external crystallites of the outer layer have a spinel-type structure and are identified either as

nickel ferrite $NiFe_2O_4$ or $Ni(Cr,Fe)_2O_4$. A higher density of crystallites identified as $NiFe_2O_4$ or NiO is nucleated in primary water and filaments of nickel oxide or hydroxide are also observed. The existence of NiO for the oxidation conditions used here is consistent with the thermodynamics stability diagram calculated for nickel base alloy [15] while the formation of nickel hydroxide was reported by several authors [15,41,44].

In both environments, the inner layer has a duplex structure with an outer part systematically poorer in Cr than the inner part lying just above the oxide/alloy interface. However, the structure and chemical composition of the inner layer depend on the oxidation environment. In particular, a thin continuous layer of chromium oxide $Cr_2O_3$ is formed at the oxide/alloy interface after exposure in hydrogenated steam while only spinel-type oxide is found after exposure in primary water. The formation of $Cr_2O_3$ in hydrogenated steam is associated with the existence of a Cr-depleted layer in the substrate which is not observed in the samples oxidized in primary water.

The existence of a continuous inner layer of $Cr_2O_3$ associated or not with a Cr-depleted layer in the substrate was previously reported in the literature for nickel-base alloys exposed to primary water at 325°C [41] or 360°C [44,45]. Other authors also report the existence of a Cr-rich (up to 80% of the metallic elements) oxide inner scale associated with a Cr-depleted layer after oxidation at 360°C [25,46] but they don't conclude on the oxide phase formed. At last, the presence of a continuous layer of a Cr-rich spinel-type oxide [20] in which discontinuous nodules of $Cr_2O_3$ may be dispersed [15,47] is also reported after exposure at 325°C. Therefore, the differences observed between our two sets of samples cannot be explained solely by an environment effect as $Cr_2O_3$ is also found in some cases after exposure in primary water. On the contrary, temperature might play a role as chromium oxide associated with a Cr-depleted layer in the substrate is mostly observed after exposure at 360°C and may result from the thermal activation of Cr diffusion in the substrate.

Such difference in the oxide scale composition is not observed on austenitic stainless steel [43]. In both environments, the oxide layer consists in magnetite and iron chromite crystallites lying on a thin continuous layer of mixed nickel and iron chromite. However, the Cr-depleted layer in the substrate is only observed on the samples exposed in primary water. On the contrary, a slightly Cr-enriched zone is found at the oxide/alloy interface after exposure in hydrogenated steam. This difference is attributed to the formation of internal and intergranular oxide penetration in the primary water exposed sample.

*4.3. Effect of microstructural parameters*

The samples used in this study are polished to mirror finish either with 1µm diamond paste or with colloidal silica suspension. The final surface state affects the crystallites density of the outer layer. More facetted crystallites and more filaments are found on the OPS polished samples after exposure in hydrogenated steam and primary water, respectively. A detailed study of the oxide layer was performed only on the steam-exposed sample. In these conditions, the thickness and composition of the inner layer are similar for both surface states but more oxide penetration are observed on the OPS finished sample.

More interestingly, TEM analyses reveal that a recrystallized layer with nanoscale grains exists in the substrate at the alloy/oxide interface for all the samples except one. The thickness of this layer ranges between 250 and 400 nm. TEM analysis performed on a sample in the as-prepared and non-oxidized state shows that this layer results from sample preparation (Fig. 14). Machining most probably induces a recrystallization process at the surface of the material which is partly removed by grinding during sample preparation before oxidation. After oxidation, chemical heterogeneities (described in part 3.3) are observed with Cr-depleted grains, oxide penetrations and sulfide precipitates. However, nodules of chromium oxides are already detected before oxidation in the as-prepared state. Similar recrystallized layers are observed by Cissé et al. [43] on austenitic stainless steel samples that were spark machined and finished by precision grinding. According to their study, this layer does not affect the nature and structure of the oxide layer but its thickness. Compared to mirror-polished samples for which this fine-grained layer is not observed, a tenfold decrease of the inner oxide thickness is measured on the precision ground samples. The difference is attributed to a faster establishment of the inner passive layer resulting from a faster diffusion of chromium in the alloy due to the presence of a high amount of short circuits for diffusion.

One sample, oxidized in primary water, does not exhibit a recrystallized layer. In this case, a dense random network of Cr-rich oxide penetrations is observed over a depth of 100 nm (Fig. 13c). Similar oxide particles identified as $Cr_2O_3$ platelets surrounded by nanocrystalline MO-structure oxide are observed at the surface and at crack walls of 20% and 26% cold-rolled Alloy 690 after exposure in primary water at 360°C [48]. At the surface, the affected depth is close to 100 nm. Similar internal oxidation is also reported for Alloy 600 exposed to hydrogenated steam at 480°C and 1 bar [49]. In this case, the material was solution-annealed for 1h at 1050°C and then water-quenched and the samples were mirror-polished with alumina suspension finish before oxidation. In both aforementioned references, the authors attribute the penetrative intragranular oxidation to the presence of short-circuits for the inward lattice diffusion of oxygen in the alloy. A high density of dislocations, coming either from

sample preparation or from the welding process, is observed in our sample as shown in Fig. 10a and may contribute to the formation of the internal intraganular oxide.

At last, the surface oxide layer is similar for the as-welded and heat-treated samples after exposure to hydrogenated steam and to primary water. In the latter case, differences are observed in terms of oxide penetrations. However, as discussed previously, these differences most probably result from a different surface state of the samples rather than an effect of the thermal treatment.

## 5. Conclusion

The oxide layer formed during corrosion of nickel-base Alloy 82 in hydrogenated steam and simulated primary water is characterized by XPS, SEM and advanced TEM techniques. For each environment, the investigations did not reveal a noticeable effect of heat treatment, test duration or surface preparation on the structure and chemical composition of the surface oxide layer. The latter exhibit the expected duplex structure with a discontinuous external layer composed of nickel ferrite oxide crystallites and a Cr-rich continuous internal layer. After exposure to hydrogenated steam, the continuous layer consists of an inner layer of $Cr_2O_3$ covered by an outer layer of $Ni(Fe,Cr)_2O_4$ whereas only $Ni(Fe,Cr)_2O_4$ is observed after exposure in primary water. However, the layer is more compact in its inner part than in its outer part. A 250-to-400 nm thick recrystallized layer resulting from sample machining and preparation is observed in the substrate at the oxide / alloy interface of most of the samples. The layer is strongly heterogeneous in terms of chemical composition with Cr-depleted grains and the presence of discrete oxide penetrations and sulfides precipitates. A entanglement of intragranular oxide penetrations is observed when a high dislocation density exists at the surface of the sample.

**Acknowledgement**

SERMA Technologies (Grenoble, France) is gratefully acknowledged for FIB TEM sample preparation. The authors thank François Jomard (GEMaC, CNRS, Univ. Versailles – St Quentin) for XPS crater depth profiling. Frédéric Miserque (CEA Saclay) is also acknowledged for fruitful discussion.

**References**


[1] H. Coriou, R. Grall, M. Le Gall, S. Vettier, “Corrosion fissurante sous contrainte de l’Inconel dans l’eau à haute température”, 3è colloque annuel de Métallurgie-Corrosion, North Holland Publishing Co., Amsterdam, Holland (1959) 1-9

[2] K. Ahluwalia, C. King, “Materials Reliability Program: Review of Stress Corrosion Cracking of Alloys 182 and 82 in PWR primary water service (MRP-220)”, EPRI Report n°1015427, Palo Alto (2007)

[3] F. Champigny, C. Amzallag, F. Chapellier, F. Vaillant, “Maintenance strategy of Inconel components in PWR primary system in France”, Proceedings of conference on vessel penetration inspection cracking and repairs, Gaithersburg, USA (2003)

[4] P. Efsing, B. Forssgren, R. Kilian "Root cause failure analysis of defected J-groove welds in steam generator drainage nozzles", Proceedings of 12th International Conference on Environmental Degradation of Materials in Nuclear Power Systems – Water Reactors”, Salt Lake City, USA (2005)

[5] P.M. Scott, “PWSCC of Nickel base alloys & mitigation in PWRs”, INL Seminar of SCC in LWRs, Idaho Falls, USA (2013)

[6] R. S. Pathania, A. R. McIlree, and J. Hickling, “Overview of Primary Water Cracking of Alloys 182/82 in PWRs,” Fontevraud V International Symposium on Contribution of Materials Investigation to the Resolution of Problems Encountered in Pressurized Water Reactors, SFEN, 2002, pp. 13–27

[7] F. Vaillant, J.M. Boursier, L. Legras, B. Yrieix, E. Lemaire, J. Champredonde, C. Amzallag, “A review of weldability and SCC behaviours of Ni-base weld metals in laboratory PWR environment”, Proceedings of 13th International Conference on Environmental Degradation of Materials in Nuclear Power Systems—Water Reactors, Whistler, USA (2007)

[8] G. Economy, R.J. Jacko, F.W. Pement, “IGSCC behavior of Alloy 600 steam generator tubing in water or steam tests above 360°C”, Corrosion 43 (1987) 727-734

[9] C. Guerre, C. Duhamel, M. Sennour, J. Crépin, M. le Calvar, “SCC crack growth rate of Alloy 82 in PWR primary water conditions – effect of a thermal treatment”, Proceedings of 15th International Conference on Environmental Degradation of Materials in Nuclear Power Systems—Water Reactors, Colorado Springs, USA (2013)

[10] E. Chaumun, J. Crépin, I. de Curières, C. Duhamel, C. Guerre, E. Héripré, M. Sennour, “Initiation of SCC crack in Nickel-based weld metals: influence of microstructural features”, Proceedings of 16th International Conference on Environmental Degradation of Materials in Nuclear Power Systems—Water Reactors, NACE, Ashville, USA (2013)

[11] M. Sennour, E. Chaumun, J. Crépin, C. Duhamel, F. Gaslain, C. Guerre, I. de Curières, “ TEM investigations on the effect of chromium content and of stress relief treatment on precipitation in Alloy 82 ”, J. Nucl. Mater. 442 (2013) 262-269

[12] H. Hänninen, P. Aaltonen, A. Brederholm, U. Ehrnstén, H. Gripenberg, A. Toivonen, J. Pitkänen, I. Virkkunen, “Dissimilar metal weld joints and their performance in nuclear power plant and oil refinery conditions”, VTT Research Notes 2347 (2006)

[13] S.M. Bruemmer, G.S. Was, “Microstructural and microchemical mechanisms controlling intergranular stress corrosion cracking in light-water-reactor systems”, J. Nucl. Mater. 216 (1994) 348-363

[14] R.W. Staehle, "Introduction to initiation", Workshop on Detection, Avoidance, Mechanisms, Modelling, and Prediction of SCC Initiation in Water-Cooled Nuclear Reactor Plants, Beaune, France (2008)

[15] M. Sennour, L. Marchetti, F. Martin, S. Perrin, R. Molins, M. Pijolat, “A detailed TEM and SEM study of Ni-base alloys oxide scales formed in primary conditions of pressurized water reactor”, J. Nucl. Mater. 402 (2010) 147-156

[16] L. Marchetti, S. Perrin, Y. Wouters, F. Martin, M. Pijolat, “Photoelectrochemical study of nickel base alloys oxide films formed at high temperature and high pressure water”, Electrochimica Acta 55 (2010) 5384-5392

[17] A. Machet, A. Galtayries, S. Zanna, L. Klein, V. Maurice, P. Jolivet, M. Foucault, P. Combrade, P. Scott, P. Marcus, "XPS and STM study of the growth and structure of passive films in high temperature water on a nickel-base alloy", Electroch. Acta 49 (2004) 3957-3964

[18] P. Combrade, P.M. Scott, M. Foucault, E. Andrieu, P. Marcus, "Oxidation of Nickel base alloys in PWR water: oxide layers and associated damage to the base metal", Proceedings of 12th International Conference on Environmental Degradation of Materials in Nuclear Power Systems—Water Reactors, TMS, Salt Lake City, USA (2005)

[19] F. Huang, J. Wang, E.H. Han, W. Ke, "Microstructural characteristics of the oxide films formed on Alloy 690 TT in pure and primary water at 325°C", Corrosion Science, 76 (2013) 52-59

[20] K. Kruska, P. Chou, O. Calonne, L. Fournier, S. Lozano-Perez, "Atom-probe tomography of surface and grain boundary oxides in Alloy 600 and Alloy 690 exposed to simulated PWR primary water", Proceedings of 12th International Conference on Environmental Degradation of Materials in Nuclear Power Systems—Water Reactors, NACE, Asheville, USA (2013)

[21] J.H. Liu, R. Mendonça, R.W. Bosch, M.J. Konstantinovic, "Characterization of oxide films formed on alloy 182 in simulated PWR primary water", J. Nucl. Mater. 393 (2009) 242-248

[22] C. de Araújo Figueiredo, R.W. Bosch, M. Vankeerberghen "Electrochemical investigation of oxide films formed on nickel alloys 182, 600 and 52 in high temperature water", Electrochimica Acta 56 (2011) 7871-7879

[23] T. M. Angeliu, G. S. Was, "The effect of chromium, carbon, and titanium on the oxidation of nickel-base alloys in high temperature water", Journal of the Electrochemical Society, 140 (1993) 1877-1883

[24] F. Carrette, M.C. Lafont, L. Legras, L. Guinard, B. Pieraggi, "Analysis and TEM examinations of corrosion scales grown on alloy 690 exposed to PWR environment", Mater. High Temp. 20 (2003) 581-591

[25] J. Panter, B. Viguier, J.M. Cloué, M. Foucault, P. Combrade, E. Andrieu, "Influence of oxide films on primary water stress corrosion cracking initiation of alloy 600", J. Nucl. Mater. 348 (2006) 213-221

[26] J.F. Moulder, W.F. Stickle, P.E. Sobol, K.D. Bomben, “Handbook of X-ray Photoelectron Spectroscopy”, Ed. J. Chastain, Physical Electronics Inc. (1992)

[27] K.S. Kim, R.E. Davis, “Electron spectroscopy of the nickel-oxygen system”, J. Electron Spectro. Rel. Phenom. 1 (1973) 251-258

[28] M.C. Biesinger, B.P. Payne, L.W.M. Lau, A. Gerson, R.S.C. Smart, “X-ray photoelectron spectroscopic chemical state quantification of mixed nickel metal, oxide and hydroxide systems”, Surf. Interface Anal. 41 (2009) 324-332

[29] M.C. Biesinger, B.P. Payne, A.P. Grosvenor, L.W.M. Lau, A.R. Gerson, R.St.C. Smart, “Resolving surface chemical states in XPS analysis of first row transition metals, oxides and hydroxides: Cr, Mn, Fe, Co and Ni”, Appl. Surf. Sci. 257 (2011) 2717-2730

[30] L. Marchetti, F. Miserque, S. Perrin, M. Pijolat, “XPS study of Ni-base alloys oxide films formed in primary conditions of pressurized water reactor”, Surf. Interface Anal. 47 (2015) 632-642

[31] H.W. Nesbitt, D. Legrand, G.M. Bancroft, “Interpretation of Ni2p XPS spectra of Ni conductors and Ni insulators”, Phys. Chem. Minerals 27 (2000) 357-366

[32] K.S. Kim, N. Winograd, “X-ray Photoelectron Spectroscopic studies of nickel-oxygen surfaces using oxygen and argon bombardment”, Surf. Sci. 43 (1974) 625-643

[33] A.P. Grosvenor, M.C. Biesinger, R.St.C. Smart, N.S. McIntyre, “New interpretations of XPS spectra of nickel metal and oxides”, Surf. Sci. 600 (2006) 1771-1779

[34] G.C. Allen, S.J. Harris, J.A. Jutson, “A study of a number of mixed transition metal oxide spinels using X-ray photoelectron spectroscopy”, Appl. Surf. Sci. 37 (1989) 111-134

[35] N.S. McIntyre, M.G. Cook, “X-ray photoelectron studies on some oxides and hydroxides of cobalt, nickel, and copper”, Anal. Chem. 47 (1975) 2208-2213

[36] N. S. McIntyre, D. G. Zetaruk, “X-ray Photoelectron Spectroscopic Studies of Iron Oxides”, Anal. Chem. 49 (1977) 1521-1529

[37] T. Yamashita, P. Hayes, “Analysis of XPS spectra of $Fe^{2+}$ and $Fe^{3+}$ ions in oxide materials”, Appl. Surf. Sci. 254 (2008) 2441-2449

[38] A. Darlinski, J. Halbritter, “Angle-resolved XPS Studies of Oxides at NbN, NbC, and Nb Surfaces”, Surf. Interf. Anal. 10 (1987) 223-237

[39] M.T. Marques, A.M. Ferraria, J.B. Correia, A.M. Botelho do Rego, R. Vilar, “XRD, XPS and SEM characterisation of Cu–NbC nanocomposite produced by mechanical alloying”, Mater. Chem. Phys. 109 (2008) 174-180

[40] N. Ohtsua, N. Masahashi, Y. Mizukoshi, “Angle resolved XPS studies on an anodic oxide formed on Ti–Nb–Sn alloy and the photo-induced change in carbon contaminants adsorbed on its surface”, Appl. Surf. Sci. 258 (2012) 6052-6055

[41] A. Machet, A. Galtayries, P. Marcus, P. Combrade, P. Jolivet and P. Scott, “XPS study of oxides formed on nickel-base alloys in high-temperature and high-pressure water”, Surf. Interf. Anal. 34 (2002) 197-200

[42] H. Lefaix-Jeuland, L. Marchetti, S. Perrin, M. Pijolat, M. Sennour, R. Molins, “Oxidation kinetics and mechanisms of Ni-base alloys in pressurised water reactor primary conditions: Influence of subsurface defects”, Corr. Sci. 53 (2011) 3914-3922

[43] S. Cissé, L. Laffont, B. Tanguy, M.C. Lafont, E. Andrieu, “Effect of surface preparation on the corrosion of austenitic stainless steel 304L in high temperature steam and simulated PWR primary water”, Corr. Sci. 56 (2012) 209-216

[44] F. Carrette, M.C. Lafont, G. Chatainier, L. Guinard, B. Pieraggi, “Analysis and TEM examination of corrosion scales grown on Alloy 690 exposed to pressurized water at 325°C”, Surf. Interf. Anal. 34 (2002) 135-138

[45] F. Delabrouille, B. Viguier, L. Legras, E. Andrieu, “Effect of the chromium content on the corrosion of nickel based alloys in primary water of pressurised nuclear reactors”, Mater. High Temp. 22 (2005) 287-292

[46] C. Soustelle, M. Combrade, P. Combrade, K. Wolski, T. Magnin, “PWSCC of alloy 600: a parametric study of surface film effects”, 9th

International Symposium on Environmental Degradation of Materials in Nuclear Power Systems, Newport Beach, USA (1999)

[47] A. Mazenc, A. Galtayries, A. Seyeux, P. Marcus, S. Leclercq, “ToF-SIMS study of the behavior of thermally oxidized films formed on nickel-based 690 alloy in high-temperature water”, Surf. Interf. Anal. 45 (2013) 583-586

[48] M.J. Olszta, D.K. Schreiber, L.E. Thomas and S.M. Bruemmer, “Penetrative Internal Oxidation from Alloy 690 Surfaces and Stress Corrosion Crack Walls during Exposure to PWR Primary Water”, 15th International Symposium on Environmental Degradation of Materials in Nuclear Power Systems, Colorado Springs, USA (2011)

[49] S.Y. Persaud, A. Korinek, J. Huang, G.A. Botton, R.C. Newman, “Internal oxidation of Alloy 600 exposed to hydrogenated steam and the beneficial effects of thermal treatment”, Corr. Sci. 86 (2014) 108–122

**Table 1:** Chemical composition (wt. %) of Alloy 82

| C | Ni | Cr | Fe | Co | Nb | Ti | Si | Mn | P | S | Cu |
|---|---|---|---|---|---|---|---|---|---|---|---|
| 0.025 | 71.7 | 19.12 | 3.07 | 0.04 | 2.41 | 0.1 | 0.07 | 2.57 | 0.004 | <0.001 | <0.01 |

**Table 2:** Binding energies for Ni $2p_{3/2}$ obtained on selected nickel oxides and nickel hydroxides

| | Main peak | | | satellite | | Minor contributions | | reference |
|---|---|---|---|---|---|---|---|---|
| | **Peak 1** | **Peak 2** | **Peak 3** | **Peak 4** | **Peak 5** | **Peak 6** | **Peak 7** | |
| **Ni** | 852.6 | - | - | 859.2 | - | - | - | [26] |
| | 852.6 | 856.3 | - | 858.6 | - | - | - | [33] |
| | 852.6 | 856.3 | - | 858.7 | - | - | - | [28] |
| **NiO** | 854.0 | 855.8 | - | 861.2 | - | - | - | [27] |
| | 854.8 | - | - | 862.1 | - | - | - | [34] |
| | 853.7 | 855.4 | - | 860.9 | - | 864.0 | 866.3 | [28] |
| **$Ni(OH)_2$** | - | 856.6 | - | 862.4 | - | - | - | [32] |
| | - | 856.2 | - | 861.2 | - | - | - | [31] |
| | - | 856.8 | - | 862.6 | - | - | - | [17] |
| | 854.9 | 855.7 | 857.7 | 860.5 | 861.5 | 866.5 | - | [28] |
| | - | 856.2 | - | 862.1 | - | - | - | [30] |
| **$NiFe_2O_4$** | 855.3 | - | - | 862.0 | - | - | - | [35] |
| | 854.8 | - | - | 861.8 | - | - | - | [34] |
| | 854.7 | 856.2 | - | 861.6 | - | 864.9 | 867.2 | [29] |
| | 855.3 | 856.8 | - | 862.0 | - | 865.7 | 868.0 | [30] |
| **$NiCr_2O_4$** | 855.7 | - | - | 860.9 | - | - | - | [34] |
| | 853.8 | 855.8 | 856.5 | 861.0 | 861.3 | 866.0 | - | [29] |
| | 854.2 | 856.4 | - | 861.7 | - | 866.3 | - | [30] |

**Figure captions:**

**Figure 1.** SEM surface observations of the oxide layers formed in hydrogenated steam: (a) as-welded, 2500h; (b) heat-treated, 2500h; (c) heat treated, 1500h; (d) as-welded, 2500h, colloidal silica finish.

**Figure 2.** (a) Ni 2p, (b) Fe 2p and (c) Cr 2p XPS spectra acquired on the as-welded sample oxidized 2500h in hydrogenated steam at 400°C.

**Figure 3.** (a) Mn 3p and (b) Nb 3d XPS spectra acquired on the as-welded sample oxidized 2500h in hydrogenated steam at 400°C.

**Figure 4.** (a) Composition depth profiles and (b) depth profiles of $Cr^0/Cr^{3+}$ and $Nb^{2+}/Nb^{5+}$ obtained from XPS on the as-welded sample exposed 2500h to hydrogenated steam. The inset in (a) is a zoom of the low concentration region.

**Figure 5.** TEM images of the oxide layer formed on samples exposed to hydrogenated steam: (a) as-welded, 2500h, 1 µm finish; (b) heat treated, 2500h, 1 µm finish; (c) heat treated, 1500h, 1 µm finish; (d) as-welded, 2500h, colloidal silica suspension finish.

**Figure 6.** (a) STEM-HAADF (Z-contrast) image acquired on the as-welded sample oxidized 2500h in hydrogenated steam at 400°C. The oxide layer and MnS particles show a darker contrast with respect to the alloy. (b) EDX compositional profile across the oxide layer and the alloy as illustrated on (a) (red dashed arrow). The STEM image and the EDX compositional profiles can be considered as representative of all samples oxidized in hydrogenated steam.

**Figure 7.** HRTEM images obtained on the oxide layer formed on samples oxidized in hydrogenated steam conditions: (a) an external large crystallite identified as $NiFe_2O_4$-structure oxide; (b) an external platelet-like crystallite identified as mixed spinel $Ni(Fe,Cr)_2O_4$-structure oxide and the top region of the continuous internal layer identified as chromite $NiCr_2O_4$-structure oxide; (c) the inner part of the continuous layer (10-15 nm) identified as chromia $Cr_2O_3$-structure oxide. Inserts are FFT diffractograms corresponding to the analyzed areas.

**Figure 8.** SEM observations of the oxide surface of primary water exposed samples:

(a) as-welded, 2500h; (b) heat-treated, 2500h; (c) heat-treated, 1500h; (d) as-welded, 2500h, colloidal silica finish.

**Figure 9.** TEM images of samples exposed to primary water: (a) as-welded sample, (b) heat-treated sample. (c) Zoom on the oxide scale of the heat-treated sample.

**Figure 10.** (a) and (b) STEM-HAADF images representative of the oxide layer formed on samples exposed to primary water showing the presence of penetrative oxidation filaments forming a band of 50-60 nm of width under the oxide continuous layer. (c-f) EDX elemental maps of oxygen, chromium, iron and nickel acquired on the framed region on (b). They show that the penetrative oxide filaments are rich in chromium and oxygen as well as the continuous layer while the external crystallite contains nickel, iron and oxygen.

**Figure 11.** (a) and (b) STEM-HAADF images representative of the oxide layer formed on the heat-treated sample exposed to primary water; (c) and (d) EDX compositional profiles across the oxide layer and the alloy as illustrated on (a): (c) corresponds to solid arrow and (d) to dashed arrow.

**Figure 12.** HRTEM images of the oxide layer formed on samples exposed to primary water: (a) external large crystallite identified as NiO-structure oxide; (b) external small crystallite identified as mixed spinel $NiFe_2O_4$-structure oxide; (c) filament oxide; (d) continuous internal layer identified as chromite $NiCr_2O_4$-structure oxide. Inserts are electron diffraction pattern in (a) and FFT diffractograms in (b), (c) and (d).

**Figure 13.** Summary of the oxide layers formed on the surface of (a) as-welded and heat-treated samples exposed to hydrogenated steam; (b) as-welded sample and (c) heat-treated sample exposed to simulated primary water.

**Figure 14.** (a) Surface state of an as-prepared non-oxidized sample and (b) associated electron diffraction pattern revealing the nanograined structure.

**Figure 1**

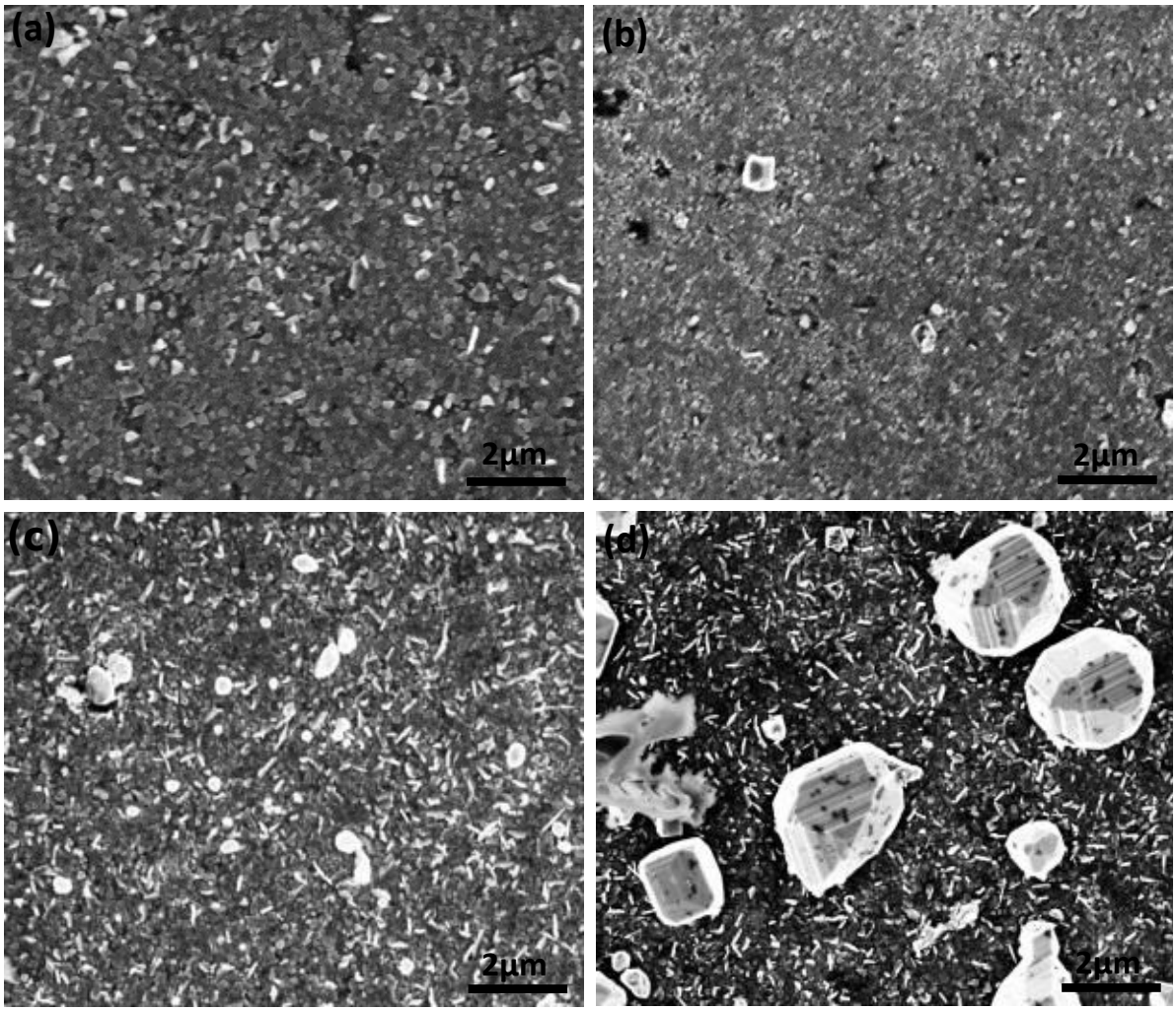

**Figure 2**

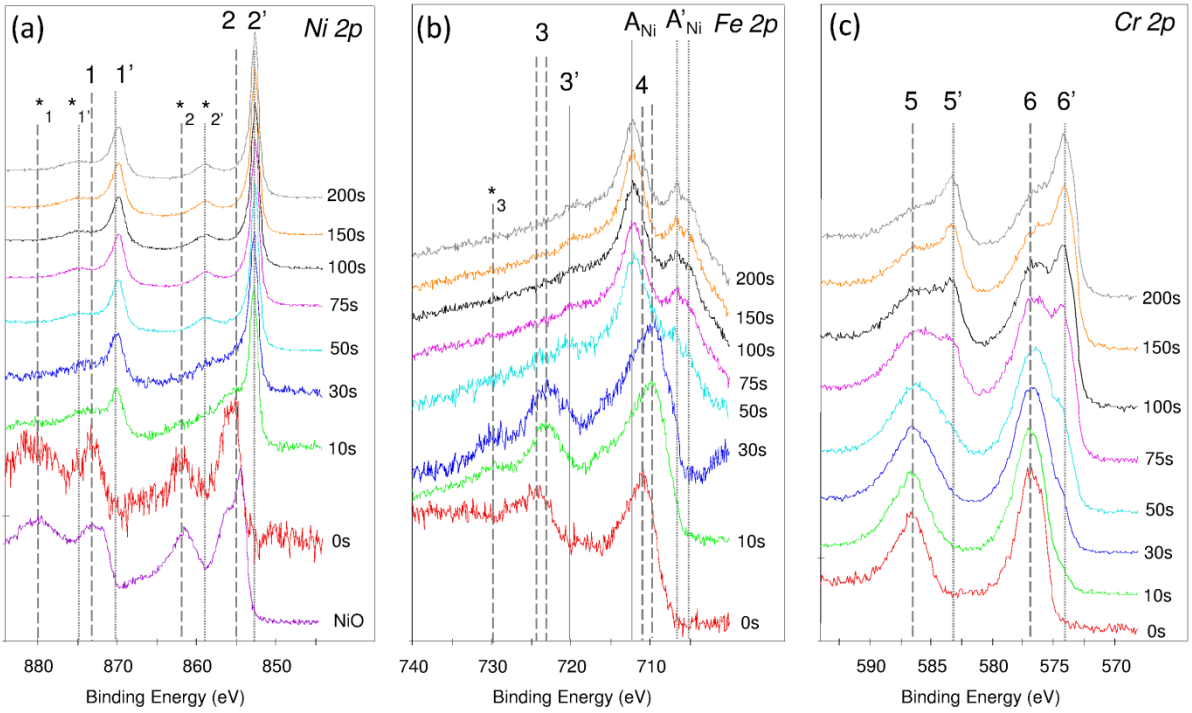
(a)
Ni 2p
1
1'
2
2'
*1
*1'
*2
*2'
200s
150s
100s
75s
50s
30s
10s
0s
NiO
880
870
860
850
Binding Energy (eV)
(b)
Fe 2p
3
3'
4
A_Ni
A'_Ni
*3
200s
150s
100s
75s
50s
30s
10s
0s
740
730
720
710
Binding Energy (eV)
(c)
Cr 2p
5
5'
6
6'
200s
150s
100s
75s
50s
30s
10s
0s
590
585
580
575
570
Binding Energy (eV)

**Figure 3**

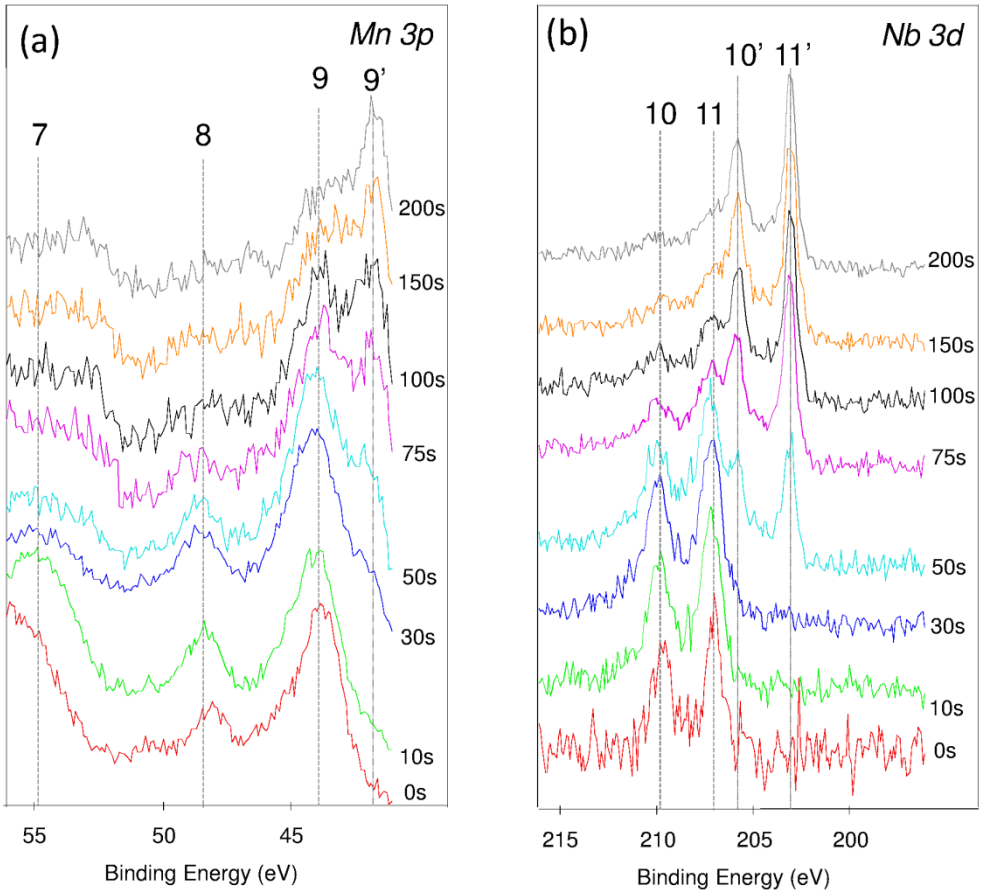
(a)
Mn 3p
7
8
9
9'
200s
150s
100s
75s
50s
30s
10s
0s
55
50
45
Binding Energy (eV)
(b)
Nb 3d
10'
11'
10
11
200s
150s
100s
75s
50s
30s
10s
0s
215
210
205
200
Binding Energy (eV)

**Figure 4**

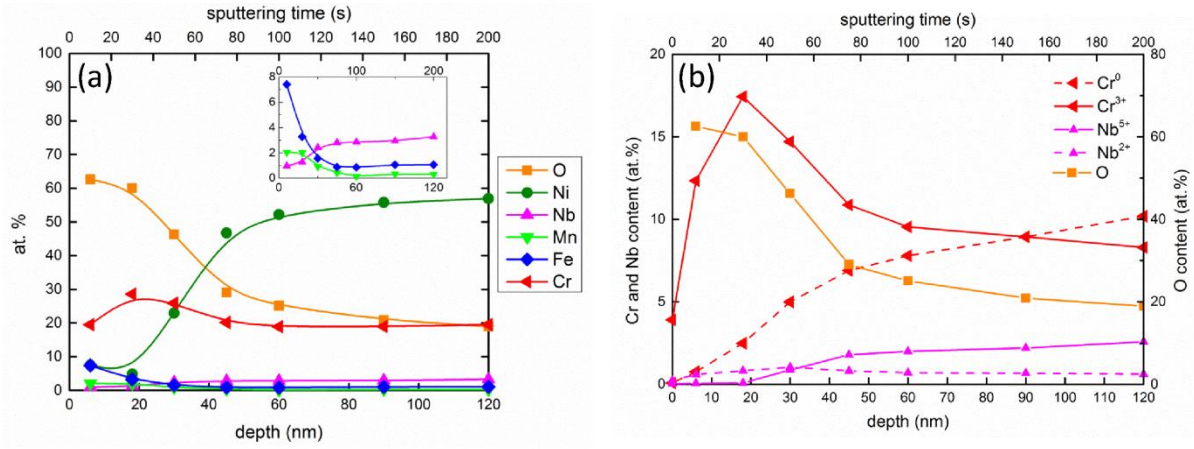
sputtering time (s)
(a)
at. %
depth (nm)
O
Ni
Nb
Mn
Fe
Cr
sputtering time (s)
(b)
Cr and Nb content (at.%)
O content (at.%)
depth (nm)
Cr0
Cr3+
Nb5+
Nb2+
O

**Figure 5**

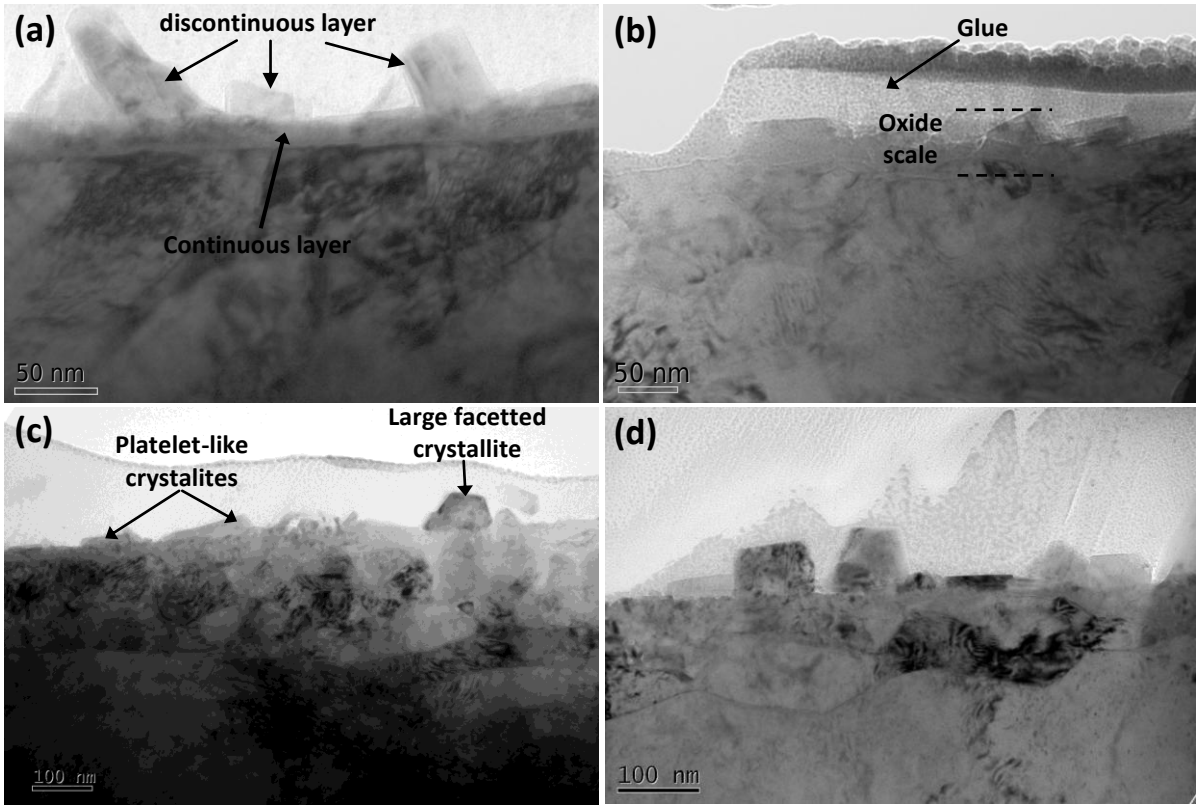
(a)
discontinuous layer
Continuous layer
50 nm
(b)
Glue
Oxide
scale
50 nm
(c)
Platelet-like
crystalites
Large facetted
crystallite
100 nm
(d)
100 nm

**Figure 6**

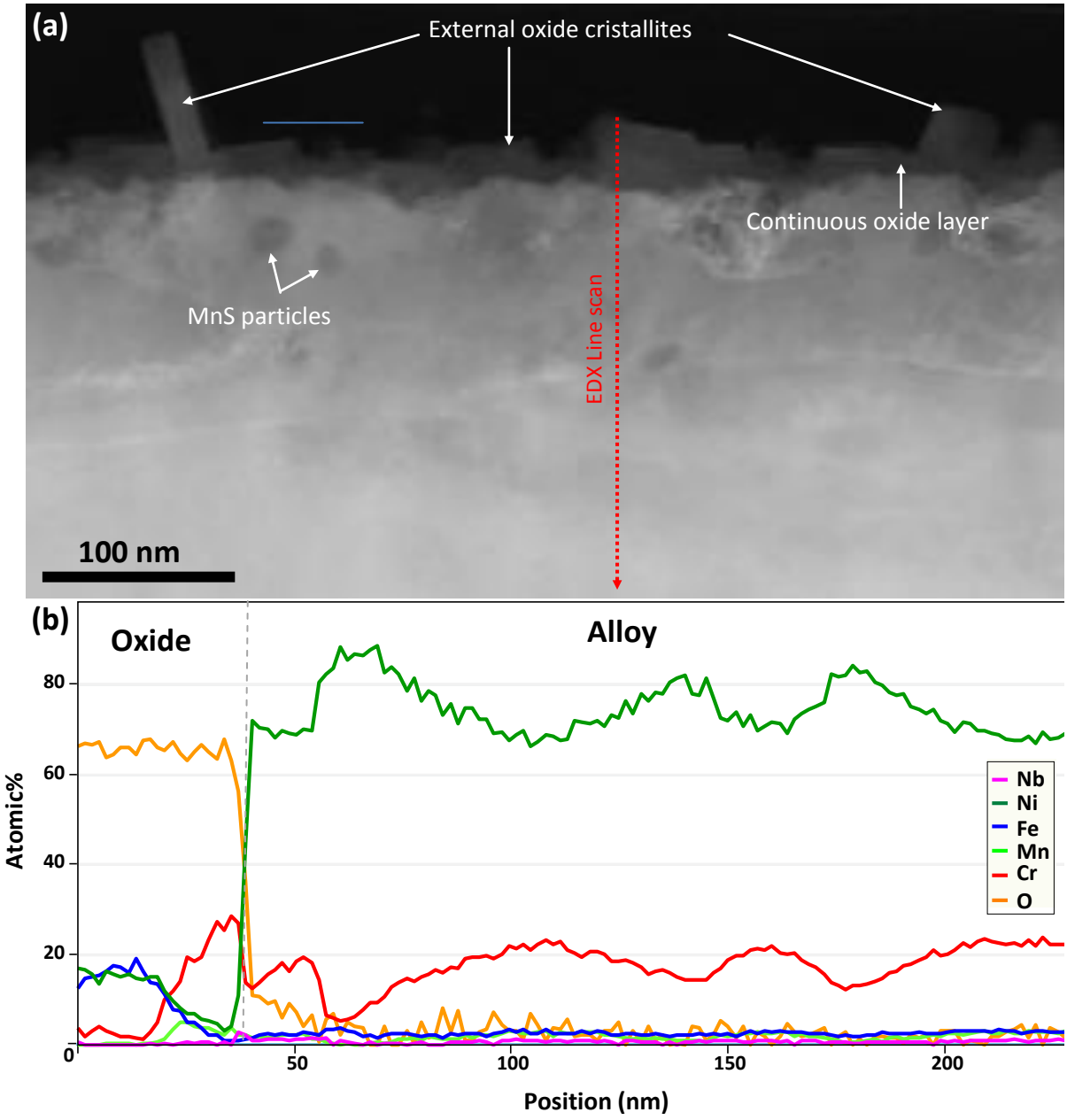
(a)
External oxide cristallites
Continuous oxide layer
MnS particles
EDX Line scan
100 nm
(b)
Oxide
Alloy
Atomic%
Position (nm)
Nb
Ni
Fe
Mn
Cr
O

**Figure 7**

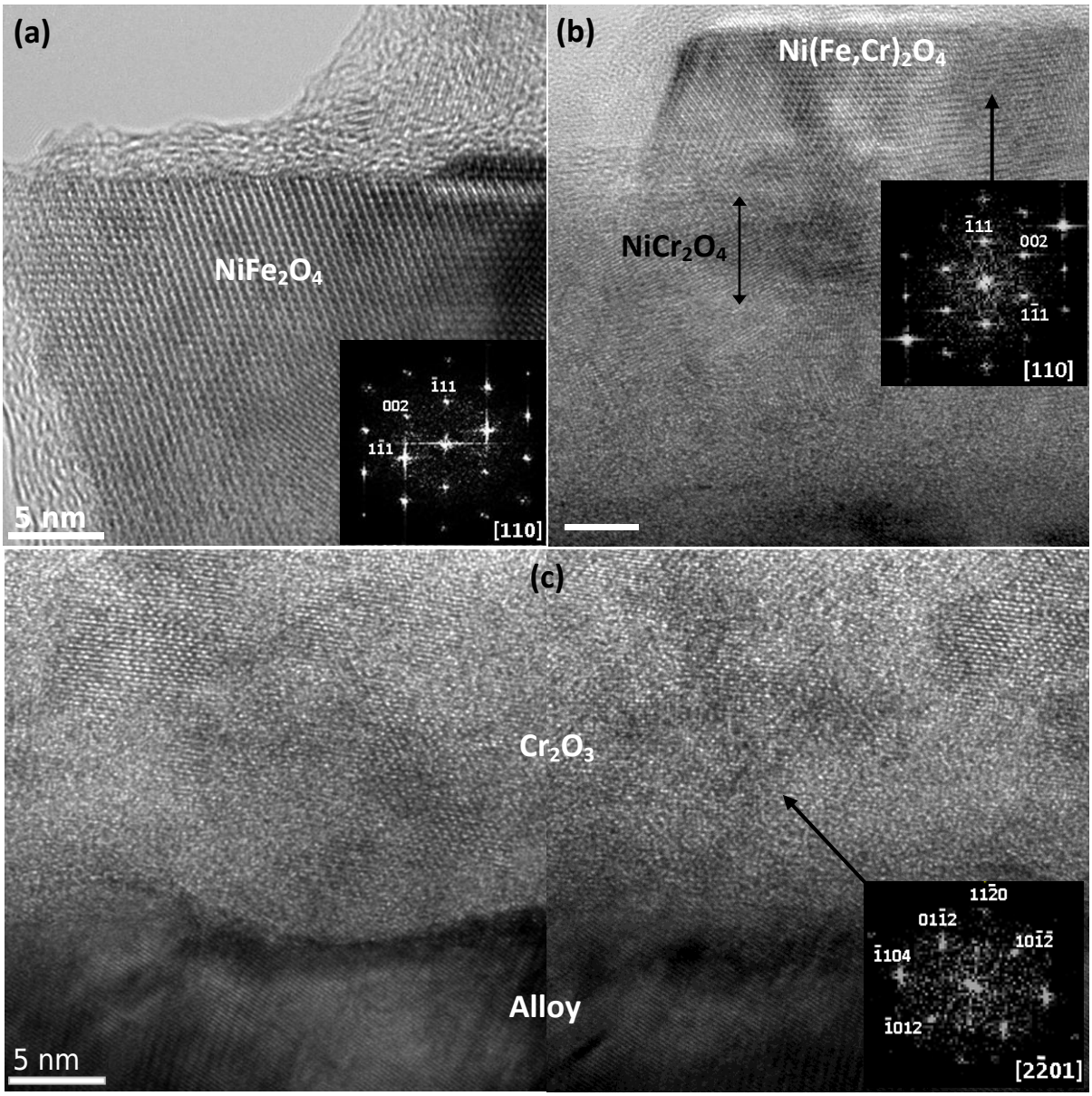
(a)
NiFe2O4
5 nm
[110]
(b)
Ni(Fe,Cr)2O4
NiCr2O4
[110]
(c)
Cr2O3
Alloy
5 nm
[2201]

**Figure 8**

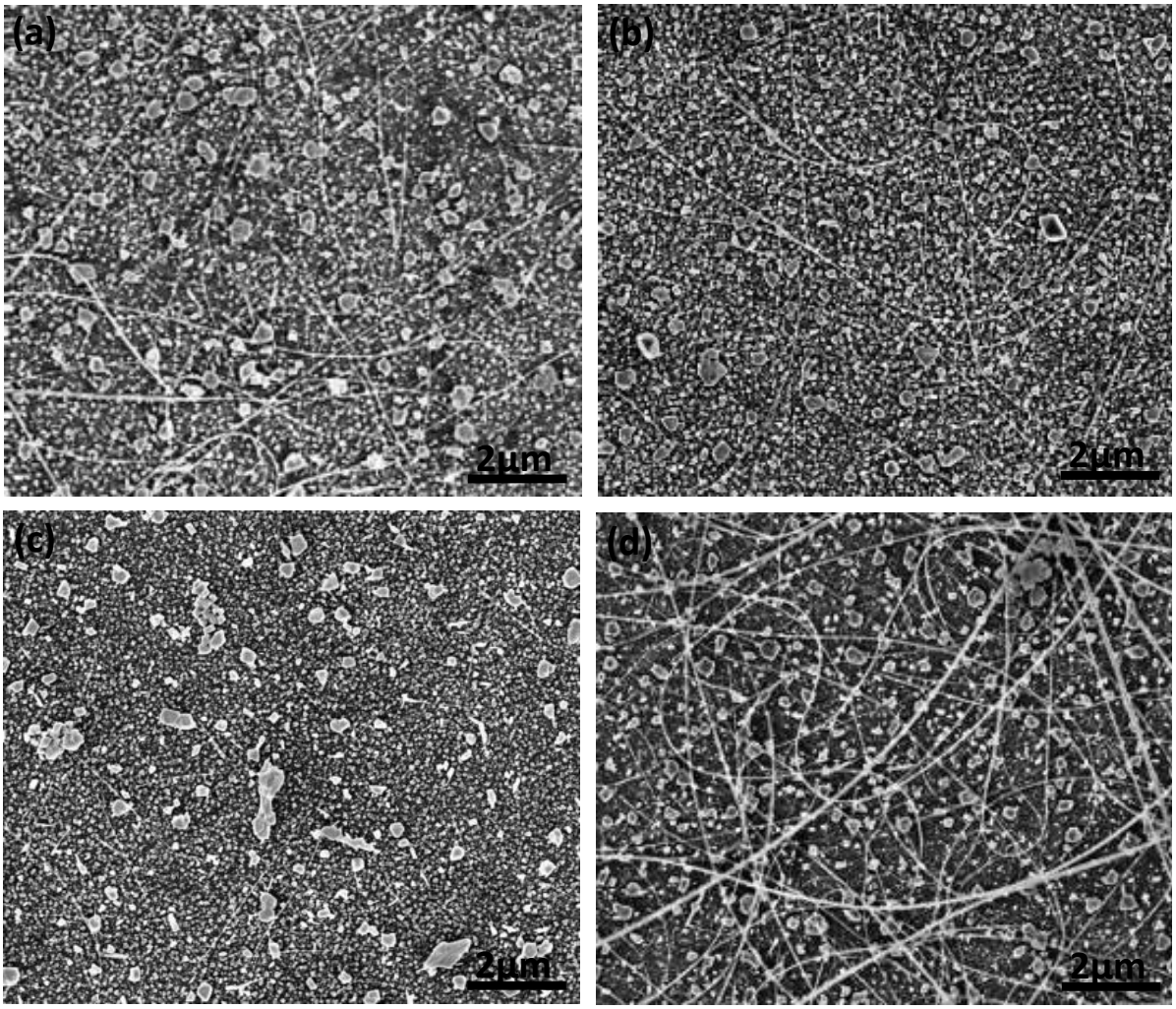

**Figure 9**

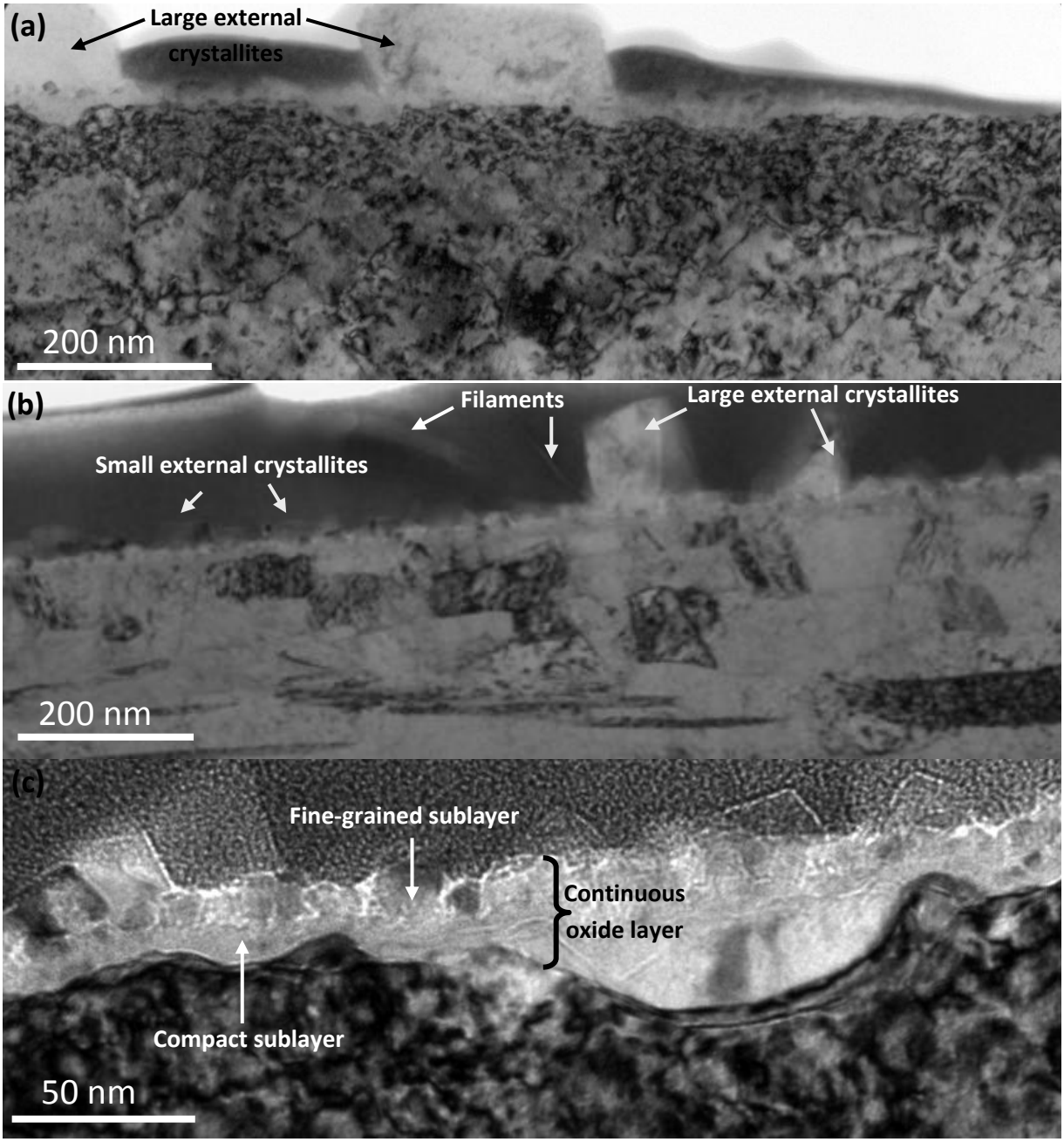
(a)
Large external crystallites
200 nm
(b)
Filaments
Large external crystallites
Small external crystallites
200 nm
(c)
Fine-grained sublayer
Continuous oxide layer
Compact sublayer
50 nm

**Figure 10**

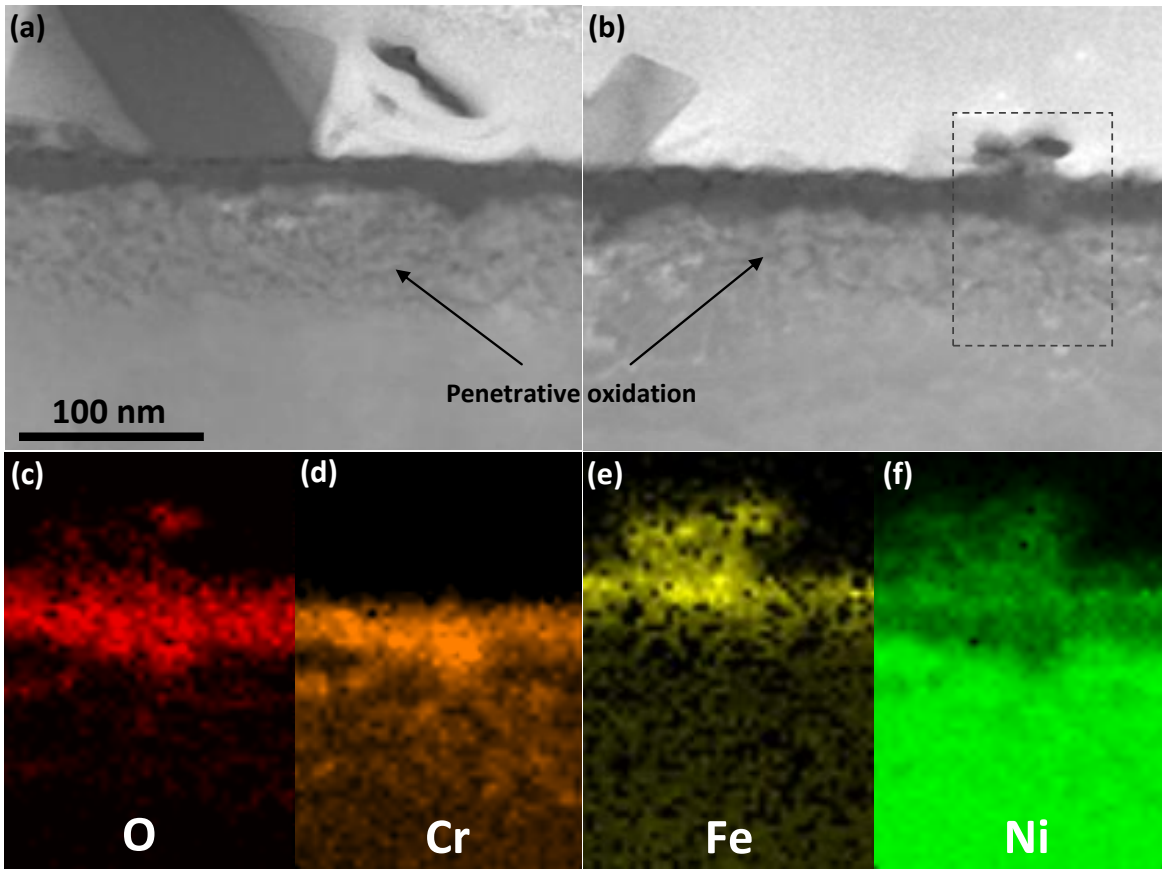

**Figure 11**

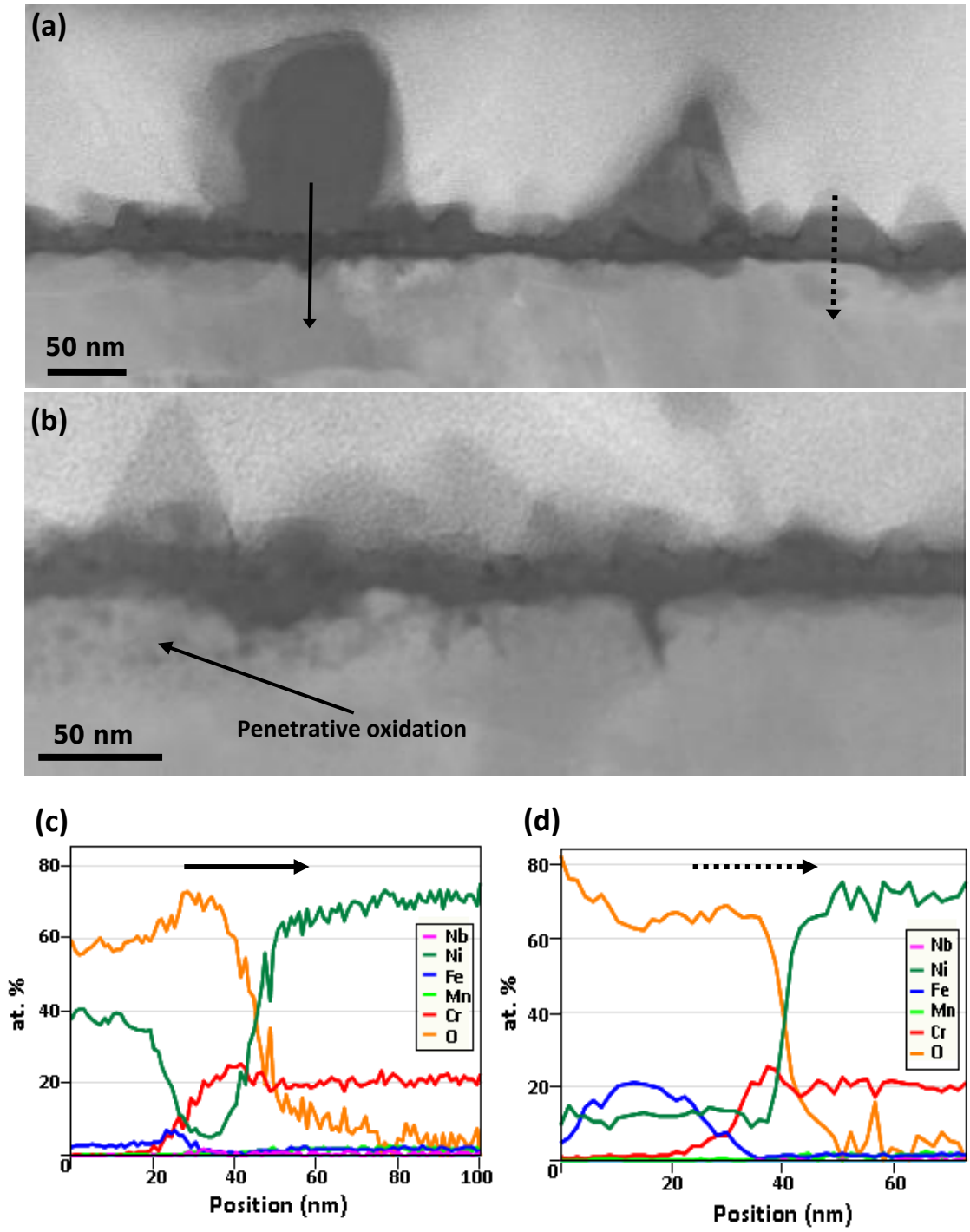
(a)
50 nm
(b)
50 nm
Penetrative oxidation
(c)
at. %
Position (nm)
Nb
Ni
Fe
Mn
Cr
O
(d)
at. %
Position (nm)
Nb
Ni
Fe
Mn
Cr
O

**Figure 12**

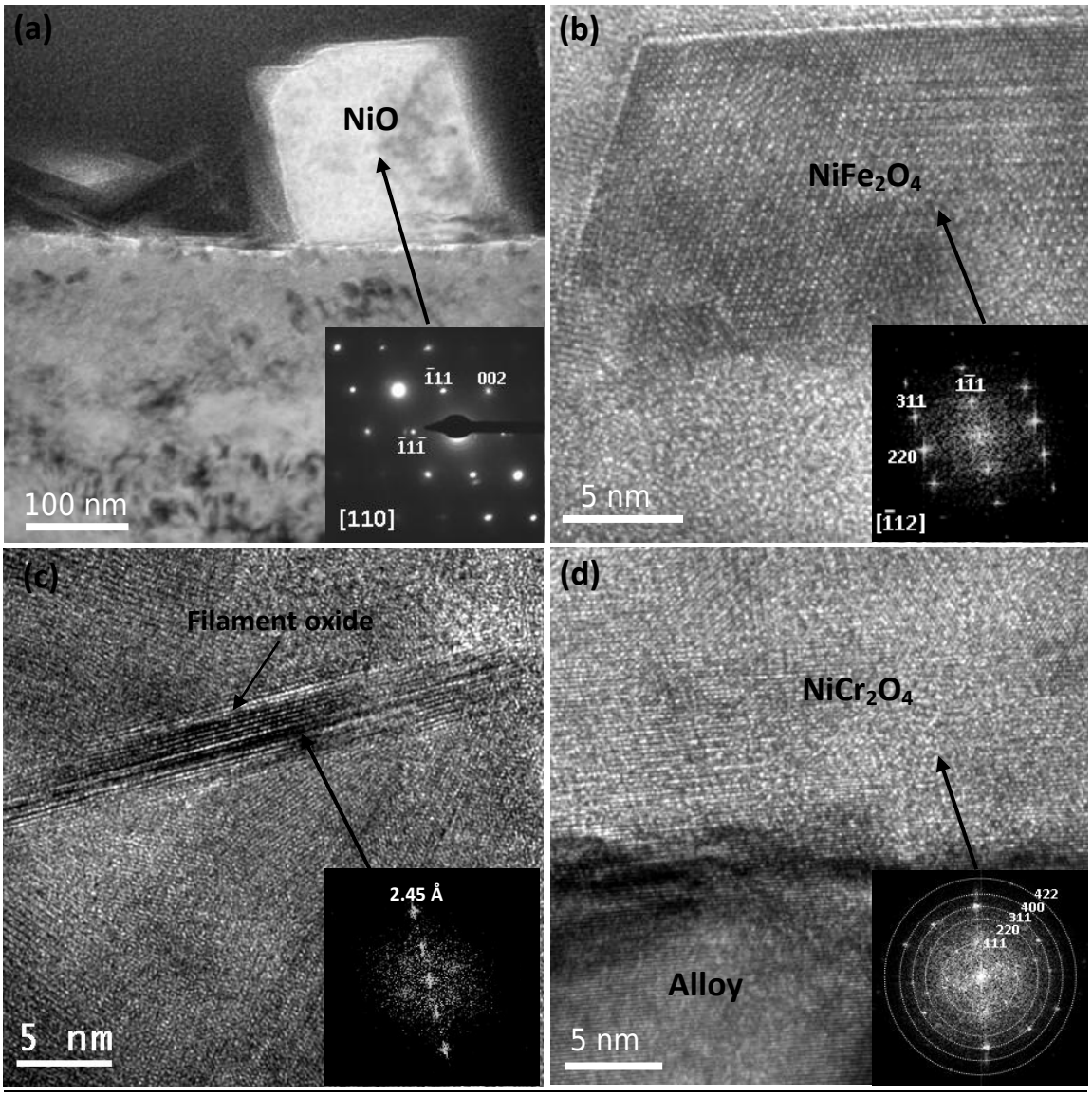
(a)
NiO
100 nm
[110]
(b)
$NiFe_2O_4$
5 nm
[112]
311
220
(c)
Filament oxide
2.45 Å
5 nm
(d)
$NiCr_2O_4$
Alloy
5 nm
422
400
311
220
111

**Figure 13**

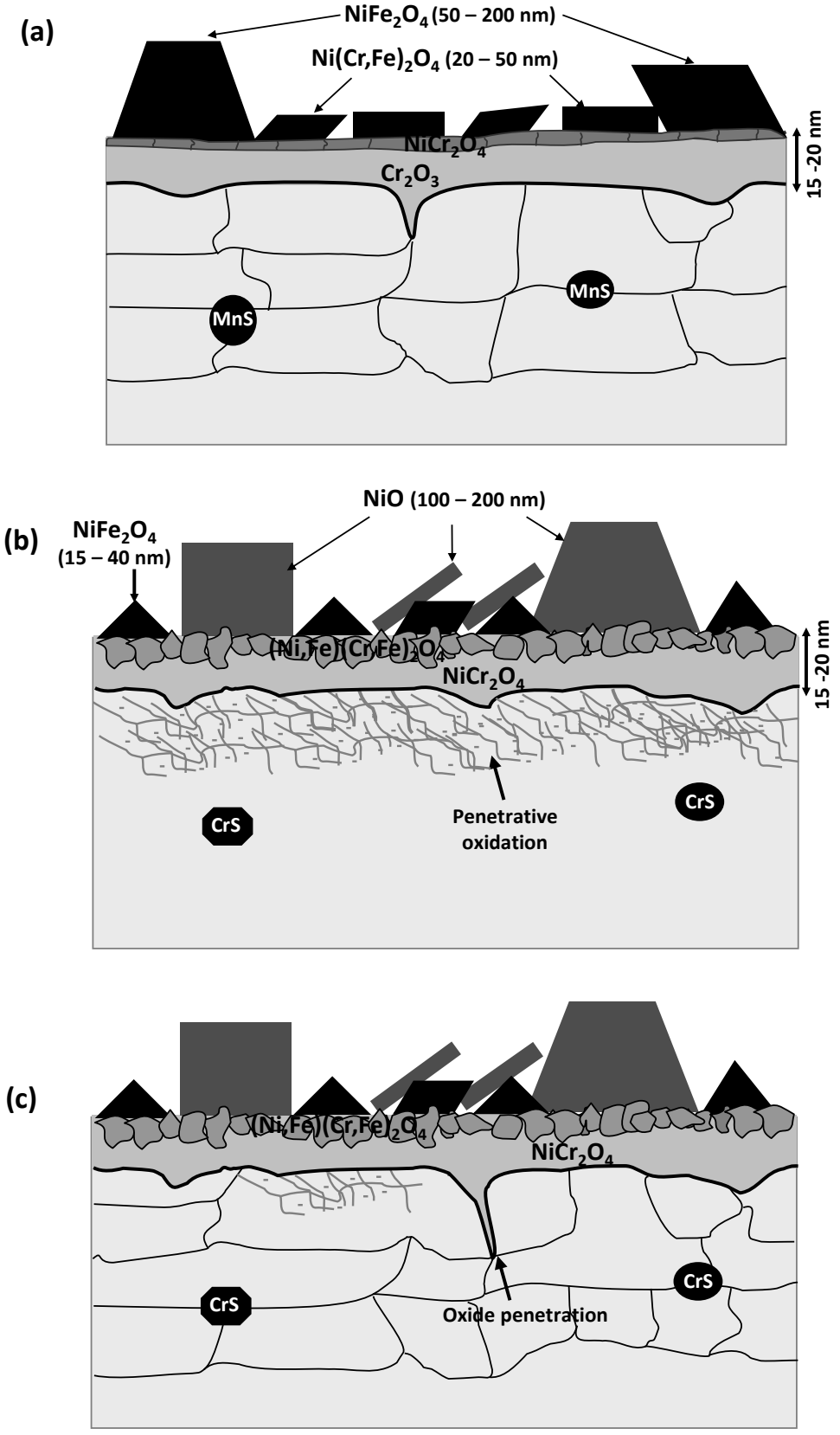
(a)
$NiFe_2O_4$ (50 – 200 nm)
$Ni(Cr,Fe)_2O_4$ (20 – 50 nm)
$NiCr_2O_4$
$Cr_2O_3$
15 -20 nm
MnS
MnS
(b)
NiO (100 – 200 nm)
$NiFe_2O_4$
(15 – 40 nm)
$(Ni,Fe)(Cr,Fe)_2O_4$
$NiCr_2O_4$
15 -20 nm
CrS
CrS
Penetrative
oxidation
(c)
$(Ni,Fe)(Cr,Fe)_2O_4$
$NiCr_2O_4$
CrS
CrS
Oxide penetration

**Figure 14**